Cerebellar Activation Bidirectionally Regulates Nucleus Accumbens Core and Medial Shell

Alexa F. D'Ambra[1], Ksenia Vlasov[1a], Se Jung Jung[1a], Swetha Ganesan[1#], Evan G. Antzoulatos[1,2b], Diasynou Fioravante[1,2b*]

[1]Center for Neuroscience, [2]Department of Neurobiology, Physiology and Behavior, University of California Davis, Davis CA 95616, United States

[a]These authors share equal authorship

[b]These authors share senior authorship

[#]Current address: Gillings School of Global Public Health, University of North Carolina

*Correspondence should be addressed to:

Diasynou Fioravante, PhD

E-mail: dfioravante@ucdavis.edu

Abstract

Although the cerebellum is now recognized as part of a long-range brain network that serves limbic functions and motivated behavior, knowledge of cerebello-limbic connectivity is limited, and nothing is known about how the cerebellum connects functionally to the nucleus accumbens (NAc). Here, we report that stimulation of cerebellar nuclei in mice of both sexes modulates spiking activity in both NAc core and medial shell with fast excitation and slower, less synchronized inhibition. Fast responses would be well poised to support rapid communication of information critical to the control of motivated behavior, whereas slower responses may be suggestive of a regulatory function, such as gain control. Tracing experiments to chart cerebellar nuclei-NAc pathways identified disynaptic pathways that recruit the ventral tegmental area (VTA) and intralaminar thalamus (Centromedial and Parafascicular nuclei) as intermediary nodes. Optogenetic activation of cerebellar axons in each of these nodes was sufficient to evoke responses in both NAc core and medial shell, albeit with distinct, node-dependent properties. These pathways and the functional connectivity they support could underlie the role of the cerebellum in motivated behavior.

Keywords

Cerebellum, nuclei, nucleus accumbens, ventral striatum, thalamus, intralaminar, VTA, connectivity, mouse, optophysiology, circuit mapping, optogenetics, motivated behavior

Introduction

The cerebellum (CB) exploits the modular organization of its circuitry to integrate information and perform complex computations. Most cerebellar research sheds light on this complexity in the context of updating and predicting motor movements (Ito, 2006). However, accumulating evidence supports cerebellar involvement in high-order non-motor functions as well (Buckner, 2013; Sokolov et al., 2017; Liang and Carlson, 2019; Hull, 2020). In humans, the CB is consistently activated during decision making, particularly during risk- or reward-based tasks (Ernst, 2002; Guo et al., 2013), and during aversive experiences and emotional learning (Moulton et al., 2014; Ernst et al., 2019). Further support for non-motor roles of the CB stems from clinical translational studies, which have linked CB dysfunction with neurodevelopmental disorders, posttraumatic stress disorder, generalized anxiety disorder, addiction, and cognitive and emotional disturbances known as cerebellar cognitive affective syndrome (Roy et al., 2013; Volkow et al., 2013; Moulton et al., 2014; Wang et al., 2014; D'Mello and Stoodley, 2015; Miquel et al., 2016; Lanius et al., 2017; Rabellino et al., 2018; Sathyanesan et al., 2019; Schmahmann, 2019). These findings are further corroborated by evidence from animal studies, which solidify a role for the CB in the processing of valence, aversion, reward, reward anticipation and omission (Wagner et al., 2017; Carta et al., 2019; Heffley and Hull, 2019; Kostadinov et al., 2019; Ma et al., 2020; Shuster et al., 2021); emotional learning and aggression (Supple et al., 1987; Sacchetti et al., 2002; Lorivel et al., 2014; Strata, 2015; Otsuka et al., 2016; Adamaszek et al., 2017; Frontera et al., 2020; Jackman et al., 2020); and motivation (Caston et al., 1998; Bauer et al., 2011; Peterson et al., 2012; Baek et al., 2022).

The ability of the CB to derive a complex repertoire of non-motor functions from its relatively invariant cellular organization is largely attributed to its diverse outputs (Reeber et al., 2013; Xiao and Scheiffele, 2018; Fujita et al., 2020; Judd et al., 2021). In addition to the heavily emphasized non-motor cerebellar influences on cortical regions (Ito, 2008; Mittleman et al., 2008; Strick et al., 2009; Watson et al., 2014; Gao et al., 2018; Brady et al., 2019; Kelly et al., 2020), functional and/or anatomical cerebellar connections with subcortical structures that are critical for cognition and emotion have also been documented (Snider and Maiti, 1976; Heath et al., 1978; Dietrichs and Haines, 1989; Rochefort et al., 2011; Fujita et al., 2020; Zeidler et al., 2020; Jung et al., 2022). Here, we focused on the nucleus accumbens (NAc), a

key limbic structure that shares reward, motivation and affective functionality with the CB (Floresco, 2015; Klawonn and Malenka, 2018). The core and medial shell (NAc_{Core}, NAc_{Med}) subregions of NAc exhibit distinct input-output organization, anatomy, and function (Groenewegen et al., 1999; Zahm, 1999; Corbit and Balleine, 2011; Ito and Hayen, 2011; Badrinarayan et al., 2012; Li et al., 2018), with roles in social behavior and reward learning that are often opposing (Floresco et al., 2018; Shan et al., 2022). Thus, the investigation of CB connections to NAc subregions could offer insights into the complexities of CB limbic functionality. Stimulation of CB cortex or deep cerebellar nuclei (DCN) modulates levels of NAc dopamine -- an important, but not exclusive, regulator of NAc functions (Dempesy et al., 1983; Albert et al., 1985; Holtzman-Assif et al., 2010; Luo et al., 2018; Holloway et al., 2019; Root et al., 2020; Zell et al., 2020; Low et al., 2021). However, how the CB connects to NAc functionally is unknown.

Here we used in vivo electrophysiology in anesthetized mice to examine the effects of DCN stimulation on spiking activity in the NAc. We provide the first evidence, to our knowledge, of an electrophysiological connection between CB and NAc, which shows NAc subregion-dependent specificity. Using viral tracing approaches, we offer insights on an anatomical blueprint of disynaptic CB-NAc connectivity, which includes nodal neurons in VTA and limbic thalamus (Centromedial nucleus, CM; and Parafascicular nucleus, PF). Through optogenetic stimulation of DCN projections to each of these nodes, we uncover circuit-dependent connectivity features that are NAc subregion-specific. These findings offer foundational insights into the contribution of the CB to limbic functions such as motivation, reward learning, and affective processing.

Results

DCN microstimulation bidirectionally modulates NAc spiking activity

To examine functional connectivity between CB and NAc, we recorded ongoing spiking activity from 546 putative single units (N = 42 mice) in NAc *in vivo* while electrically microstimulating the DCN (Fig. 1A). We primarily targeted the lateral DCN, activation of which has been shown to modulate levels of dopamine in NAc (Holloway et al., 2019; Low et al., 2021). In a subset of experiments, post-hoc analysis localized the bipolar stimulating electrode in the interposed DCN, and these data were included in our analyses. Stimulation of DCN with

five 100-μA current pulses at 200 Hz (total stimulus duration: 25 ms) evoked bidirectional modulation of NAc spiking activity (Fig. 1B). Across all recorded units, average spiking initially increased to 12.8 ± 0.4 spikes/s from a pre-stimulus baseline of 10.4 ± 0.5 spikes/s, followed by a modest, slow-recovering decrease to 9.8 ± 0.3 spikes/s. Because of jitter in response latency across neurons, the average spiking rate is an underrepresentation of the true magnitude of modulation, which is more accurately reflected in the average maximum activity. In response to stimulation, average maximum activity increased to 20 ± 0.6 spikes/s for all recorded single-units (t-test for paired samples: $t_{1017} = -33$; $p < 0.001$), followed by a decrease to an average minimum of 4 ± 0.3 spikes/s ($t_{1017} = 35.7$; $p < 0.001$) (n = 1018 units x stimulation sites). Further analysis identified three distinct response-types: excitatory (defined as firing rate increase >3σ above the baseline) (Fig. 1C), inhibitory (defined as firing rate decrease >1σ below the baseline for 3 consecutive time bins) (Fig. 1D), and mixed (both excitatory and inhibitory) (Fig. 1E).

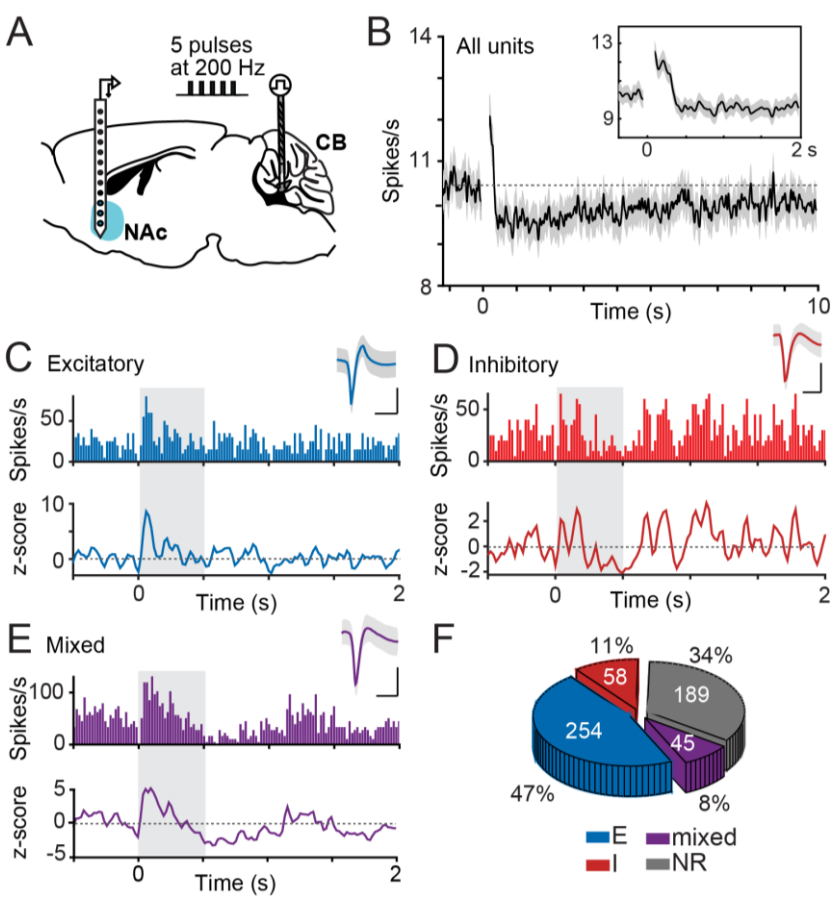

Figure 1. Cerebellar stimulation effectively elicits excitatory and inhibitory responses in nucleus accumbens. A, Schematic diagram of recording setup. Stimulation protocol consisted of 10 trials (inter-trial interval: 15 s) of five 100-μA, 0.5-ms pulses at 200 Hz. NAc: nucleus accumbens; CB: cerebellum. **B**, Average spiking activity (spikes/s) across all recorded units (N = 42 mice). Inset shows zoom-in of first two seconds after stimulation. **C**,**D**,**E**, Examples of excitatory (**C**), inhibitory (**D**), and mixed (**E**) modulation in the NAc. *Top,* Peri-stimulus time histogram (PSTH) (10-ms bins) of the average firing rate across 10 trials. *Bottom,* Baseline-normalized firing rate (z-score) across time. *Inset*, Example average waveform of putative single unit. Scale bars: 1 ms, 10 μV. Shaded area marks response window. **F,** Distribution of response types elicited in NAc by DCN stimulation. *Blue*: Excitatory (E), *Red*: inhibitory (I), *Purple:* mixed, *Gray*: non-responders (NR). Number of recorded units per response-type (*white*) and corresponding percentages are shown.

Of the 546 recorded NAc neurons, 66% responded to DCN stimulation, with most (47%) displaying an excitatory response (Fig. 1F). An inhibitory response was elicited in 11% of neurons, whereas a smaller fraction (8%) displayed mixed responses. The average excitatory response amplitude was 349 ± 15% of baseline, and the average inhibitory response amplitude was 30 ± 2% of baseline.

Effects of DCN microstimulation on NAc core and medial shell spiking activity

The NAc is divided into two distinct subregions: a core subregion (NAc_{Core}) surrounded by an outer subregion, the medial aspect of which is known as the medial shell (NAc_{Med}). Each of these subregions has unique microanatomical, functional and connectivity features (Floresco, 2015; Salgado and Kaplitt, 2015). We aimed to examine whether the difference in proportions (i.e., prevalence) between DCN-evoked excitatory and inhibitory responses in NAc stemmed from regional differences (core vs. medial shell) at NAc recording sites. Our axial multi-electrode array approach enabled recordings from multiple NAc sites in both NAc_{Core} and NAc_{Med} (Fig. 2A). Out of 169 neurons we recorded in NAc_{Core}, more than half (53%) responded with excitatory modulation to 100-μA stimulation of at least one site in DCN, while 8% responded with inhibitory modulation, and another 8% with mixed modulation (Fig. 2B *left*). Similarly, out of 377 neurons we recorded in NAc_{Med}, 44% responded to DCN stimulation with excitation, 12% with inhibition, and 8% with mixed modulation of spiking activity. The frequency distributions of these response-types in NAc_{Core} and NAc_{Med} were not significantly different ($\chi^2_{(3)} = 4.7$, $p = 0.19$).

We then examined whether the amplitude of excitatory and/or inhibitory responses varied between NAc_{Core} and NAc_{Med} (Figs. 2C-D). For this analysis, the excitatory and inhibitory components of mixed responses were considered together with the excitatory and inhibitory response types, respectively. In both NAc_{Core} and NAc_{Med}, DCN stimulation elicited significant excitatory modulation of firing rate (mean ± sem, spikes/s in NAc_{Core}: baseline: 12.2 ± 1.1, peak excitatory response: 52.2 ± 2.5, paired $t_{162} = -24.2$, $p < 0.0001$; in NAc_{Med}: baseline: 7.9 ± 0.6, peak excitatory response: 42.2 ± 1.5, paired $t_{267} = -32.4$, $p < 0.0001$), which did not differ between subregions (% baseline: NAc_{Core}: 856.2 ± 79.2, NAc_{Med}: 978.8 ± 62.5, $t_{429} = -1.2$, $p = 0.23$). Similarly, both NAc_{Core} and NAc_{Med} showed significant inhibitory modulation (mean ± sem, spikes/s in NAc_{Core}: baseline: 24.3 ± 3.9, peak inhibitory response: 4.0 ± 2.3, paired t_{42} =

144 9.7, $p < .0001$; in NAc_{Med}: baseline: 22.1 ± 1.6, peak inhibitory response: 1.3 ± 0.4, paired t_{92} =
145 15.5, $p < 0.0001$), which did not differ between subregions (% baseline: NAc_{Core}: 4.3 ± 2.1,
146 NAc_{Med}: 2.6 ± 0.8, $t_{134} = 0.9$, $p = 0.36$)(p-values corrected for multiple comparisons). These
147 results suggest that cerebellar signals are equally likely to reach NAc_{Core} and NAc_{Med}. Upon
148 further inspection, we found that irrespective of subregion, the baseline firing rate of excitatory
149 responses was significantly lower than the baseline of inhibitory responses ($F(1,563) = 88$, $p <$
150 0.001). Differences in baseline between excitatory and inhibitory responses could arise from
151 potentially different NAc cellular properties, although the fact that neurons with elevated firing
152 rates are more likely to satisfy our criterion for inhibitory responses should also be considered.

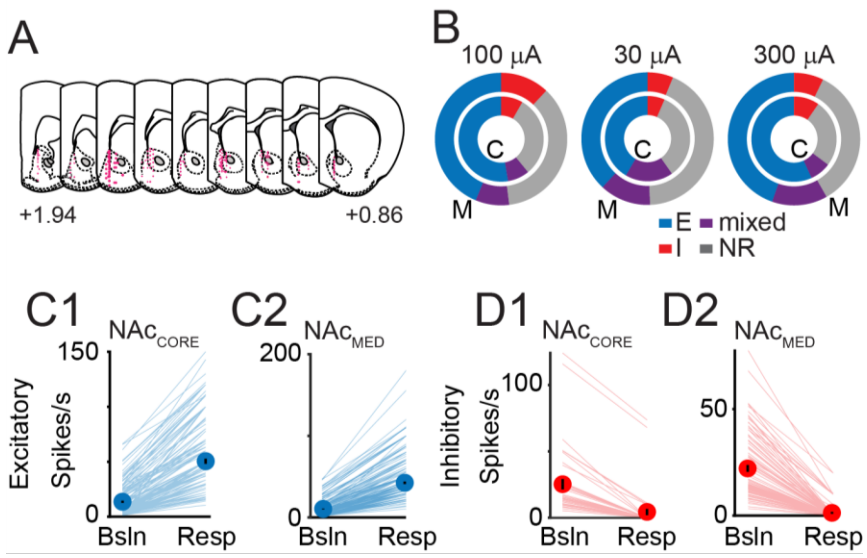

Figure 2. Nucleus accumbens responses to cerebellar stimulation. A, Recording sites in nucleus accumbens core (NAc_{Core}) and medial shell (NAc_{Med}). Numbers indicate distance (in mm) from bregma. **B,** Distribution of response types elicited by 30-, 100-, or 300-µA DCN stimulation. N_{30} = 14 mice, N_{100} = 42 mice, N_{300} = 40 mice. Outer ring (M): NAc_{Med}; inner ring (C): NAc_{Core}. *Blue:* excitatory (E), *Red*: inhibitory (I), *Purple:* mixed, *Gray:* non-responders (NR). **C,** Comparison between average baseline (Bsln) and peak firing rate (Resp) elicited by 100-µA DCN stimulation for excitatory responses in NAc_{Core} (**C1**) and NAc_{Med} (**C2**). Group averages (± SEM) are overlaid onto lines representing single units. **D1**,**2**, Same as C but for inhibitory responses.

153 **Differential and non-linear dependence of NAc responses on DCN stimulation**
154 **intensity**

155 To further probe the functional connectivity between DCN and NAc, we assessed the
156 effectiveness of DCN microstimulation at two more intensities, 30 µA and 300 µA, in addition to
157 100 µA (Fig. 2B; *middle* and *right*). In NAc_{Core}, the proportion of excitatory responses changed
158 from 42% (with 30 µA stimulation) to 53% (with 100 µA), to 57% (with 300 µA); the proportion

159 of inhibitory responses changed from 7% (30 μA) to 8% (100 μA) to 10% (300 μA); and finally,
160 the proportion of mixed responses changed from 18% (30 μA) to 8% (100 μA) to 8% (300 μA).
161 Contingency table analysis did not find a significant effect of stimulation intensity on the
162 frequency distribution of response-types in NAc_{Core} ($\chi^2_{(6)} = 9.4$; $p = 0.15$). In NAc_{Med}, the
163 proportion of excitatory responses changed from 38% (30 μA) to 44% (100 μA) to 45% (300
164 μA); the proportion of inhibitory responses changed from 6% (30 μA) to 12% (100 μA) to 7%
165 (300 μA); and the proportion of mixed responses changed from 13% to 8% to 14%. The effect
166 of stimulation intensity on the frequency distribution of response-types in NAc_{Med} was
167 statistically significant ($\chi^2_{(6)} = 13.6$; $p < 0.05$), suggesting that the NAc subregions displayed
168 differential sensitivity to the intensity of DCN microstimulation. For both NAc subregions, the
169 prevalence of the different response-types did not change proportionally to the ~3-fold change
170 in stimulation intensity, which suggests non-linear dependence to stimulation intensity.

171 **The bidirectional NAc modulation is not a reflection of topographical DCN organization**

172 In our experiments we used bipolar stimulation electrodes to contain the spread of
173 electrical current at DCN stimulation sites. To confirm that the stimulation was indeed
174 localized, we examined the likelihood of NAc neurons that responded to stimulation of
175 individual DCN sites to also respond to adjacent stimulation sites along anatomical axes in the
176 same experiment (Fig. 3A1-2). We found that the probability of a NAc_{Core} neuron that
177 responded to stimulation of a DCN site to also respond to stimulation of a site ~100 μm away
178 dropped by 66%. In NAc_{Med}, this probability dropped by 33%. The subregion-dependent
179 difference in the likelihood of adjacent DCN sites to evoke a response in the same neuron
180 most likely reflects differences in the architecture of the neural circuits. Regardless of the
181 difference between NAc subregions, the probability decrease is consistent with localized
182 stimulation.

183 Given that DCN stimulation appeared spatially restricted, could the observed differences
184 in NAc response-types arise from regional differences within DCN? To address this question,
185 we examined whether there was topographical clustering of DCN sites with respect to their
186 effectiveness to evoke significant excitatory or inhibitory responses in NAc_{Core} and/or NAc_{Med}.
187 We did not find indications of such clustering (Fig. 3B1-3, C1-3), which argues against
188 topographical organization of lateral/interposed DCN with respect to NAc response types.

Using a similar approach, we examined whether there was topographical clustering of sites with excitatory and/or inhibitory responses within NAc subregions, but we did not find evidence for any such organization either (not shown).

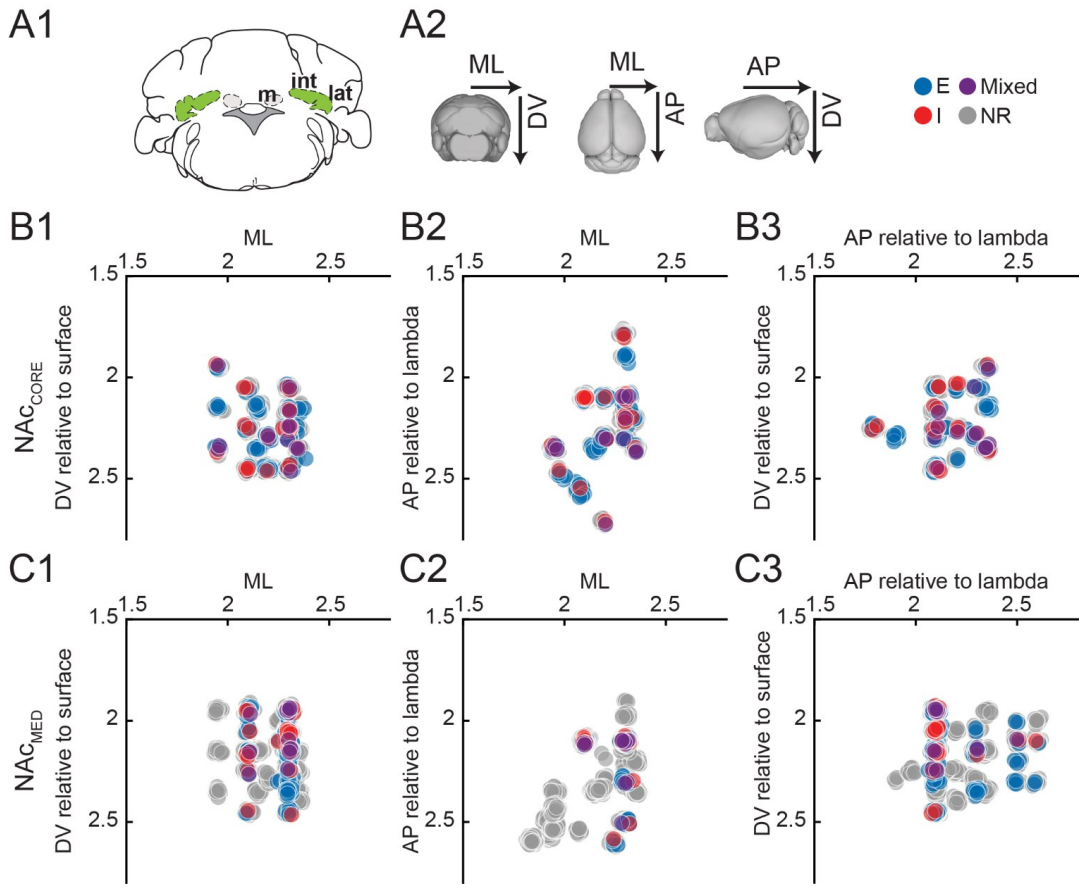

Figure 3. The distribution of response-types in nucleus accumbens subregions is not due to topographical specialization within deep cerebellar nuclei. A, The lateral (lat) or interposed (int) DCN (**A1**) was electrically stimulated. M: medial n. **A2,** Demarcation of anatomical planes: ML: medio-lateral; DV: dorsoventral; AP: antero-posterior. **B,C,** Stereotactic coordinates of DCN stimulation sites in ML-DV (B1,C1), ML-AP (B2,C2), and AP-DV (B3,C3) planes. Colored dots denote sites that evoked excitatory (excit.: *blue*), inhibitory (inh.: *red*), mixed (*purple*) or no responses (NR: *gray*) in NAc_{Core} (B1-3) and NAc_{Med} (C1-3).

Anatomical blueprint of DCN-NAc connectivity

There are no direct, monosynaptic connections between DCN and NAc (Allen Brain Atlas, and our own observations); we therefore hypothesized the existence of at least disynaptic anatomical pathways between the two areas. To test this hypothesis, we adopted a 2-pronged approach. First, we combined injection of a retrograde tracer (cholera toxin subunit

B (ctb) -640 or -568) in NAc with injection of an anterograde viral tracer (AAV9-CAG-GFP) in DCN to identify areas of overlap (nodes) in a putative disynaptic CB-NAc circuit (Fig. 4A,B) (N = 6 mice). Histological processing and high-resolution confocal imaging of brain sections revealed two regions of overlap between ctb-filled neurons that project to NAc and GFP-labelled DCN axonal projections: the VTA and limbic thalamus (Fig. 4C,D). In VTA, most areas of overlap localized medially and caudally and involved both TH+ (dopaminergic) neurons (Fig. 4C) and TH- neurons. In the thalamus, we found areas of overlap in centromedial (CM) and parafascicular (PF) intralaminar nuclei (Fig. 4D). We found overlap in these same regions also when DCN injections were restricted to the lateral cerebellar nucleus only (Fig. 4E,F). These results are consistent with the existence of a disynaptic DCN-NAc anatomical circuit and point to VTA, and CM and PF thalamic nuclei, as putative circuit nodes.

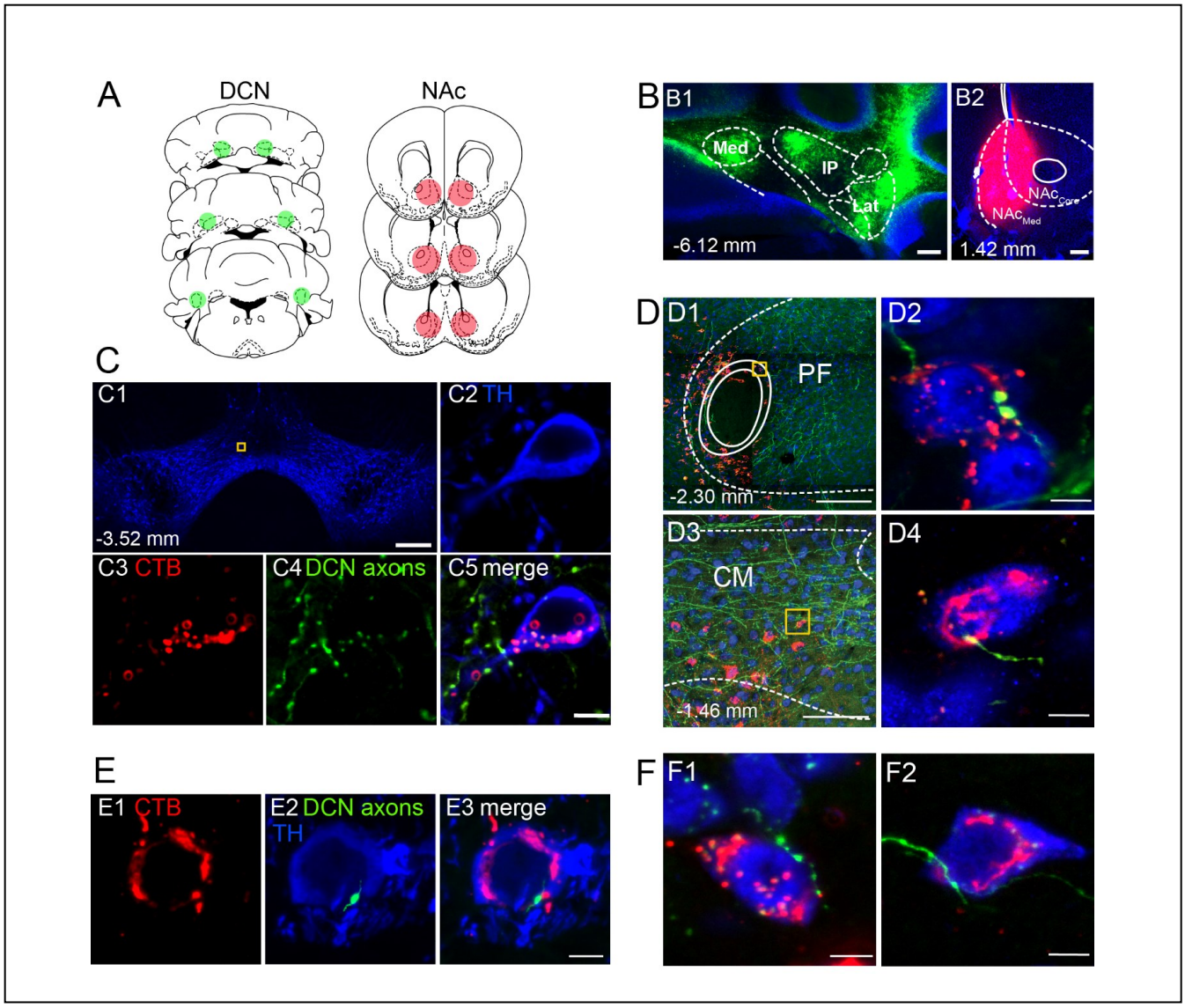

Figure 4. **Co-localization of nucleus accumbens-projecting neurons with cerebellar projections in VTA and intralaminar thalamus**. **A**, Schematic diagrams of stereotactic injections in DCN and NAc. **B1**, Expression of GFP at DCN injection sites. **B2**, Ctb-Alexa 568 injection site in NAc. **C**, Overlap of ctb-labeled NAc projectors and DCN axons in VTA. **C1**, VTA identification through TH immunostaining. **C2**, TH+ neuron. **C3**, Retrograde ctb-Alexa 568 labelling in NAc-projecting cell. **C4**, GFP-expressing DCN axons. **C5**, C2-C4 merged. **D**, Overlap of ctb retrograde label (red) in NAc projectors (blue; NeuN) and GFP-expressing DCN axons (green) in intralaminar thalamic nuclei. **D1**-**D2**, Overlap in parafascicular (PF) n. **D3**-**D4**, Overlap in centromedial (CM) n. Yellow boxes in C1,D1,D3 denote zoom-in areas depicted in C2-C5, D2 and D4, respectively. **E**-**F**, Airyscan confocal images from experiments similar to **A** but with only lateral DCN injected with AAV-GFP. **E1**, Ctb-labeled (red) NAc-projecting cell in the VTA. **E2,** TH+ cell (blue) with overlapping GFP-labeled axonal projection (green) from lateral DCN. **E3,** E1-2 merged. **F1**, GFP-labeled axon from lateral DCN (green) overlaps with ctb-labeled (red) NAc-projecting cell (blue: NeuN) in the PF n. **F2,** Same as in F1 but for neuron in the CM n. Scale bars: B1-2,C1,D1: 200 μm; C2-C5,D2,D4,E1-3,F1,F2: 5 μm; D3: 100 μm. N = 6 mice. Numbers denote distance from bregma.

To confirm these observations through an independent approach, we performed AAV1-mediated anterograde transsynaptic tracing experiments (Zingg et al., 2017) via stereotactic injections of AAV1-Cre in DCN and AAV-FLEX-tdTomato in VTA or limbic thalamus (Fig. 5A,B) (N = 4 mice). This approach relies on the transsynaptic transfer of Cre to postsynaptic neurons, which, once infected with a floxed fluorophore, become fluorescently labeled. With this method, we confirmed the existence of neurons receiving CB input in VTA (Fig. 5C1,C2) and CM, PF intralaminar thalamus (Fig. 5D1,D2). Importantly, we were able to localize their labeled axonal projections in NAc, in both NAc_{Core} and NAc_{Med} (Fig. 5C3,D3). We observed similar patterns of cell labeling and projections to the NAc_{Core} and NAc_{Med} when AAV1-Cre was injected in lateral DCN only (Fig. 5E,F) (N = 3 mice). These findings chart a blueprint of disynaptic DCN-NAc connectivity and could provide an anatomical foundation for our newly discovered DCN-NAc functional connection.

Photostimulation of DCN axonal projections in nodes supports the existence of disynaptic circuits between cerebellum and NAc

Our combined electrophysiological and neuroanatomical data point to the existence of neural circuits connecting the CB to the NAc_{Core} and NAc_{Med}, with putative nodal regions in VTA and/or intralaminar thalamus. We sought to determine whether these anatomically defined nodes are also functional nodes serving CB-NAc connectivity. To this end, we performed additional electrophysiological experiments combined with optogenetic stimulation of DCN projections in the putative nodes (Figs. 6,7). We expressed channelrhodopsin (ChR2) in DCN projection neurons through viral injection (Figs. 6A,6B) and recorded responses in NAc_{Core} and NAc_{Med} following photostimulation of DCN axons (10 pulses at 20 Hz, 10 mW at

230 fiber tip) in VTA (Fig. 6C1,C2), CM (Fig. 6D1,D2), or PF (Fig. 6E1,E2). All DCN nuclei were
231 injected in order to maximize ChR2 expression and the chances of successful stimulation of
232 projections.

233 As with electrical microstimulation of DCN sites, targeted photostimulation of ChR2-
234 expressing DCN axons in each of the three putative nodes modulated spiking activity in both
235 NAc_{Core} and NAc_{Med} (example units in Fig. 6C2,D2,E2; group averages in Fig. 7A1,B1,C1),
236 establishing the VTA, CM and PF as functional nodes of the CB-NAc circuitry. Figure 7 shows

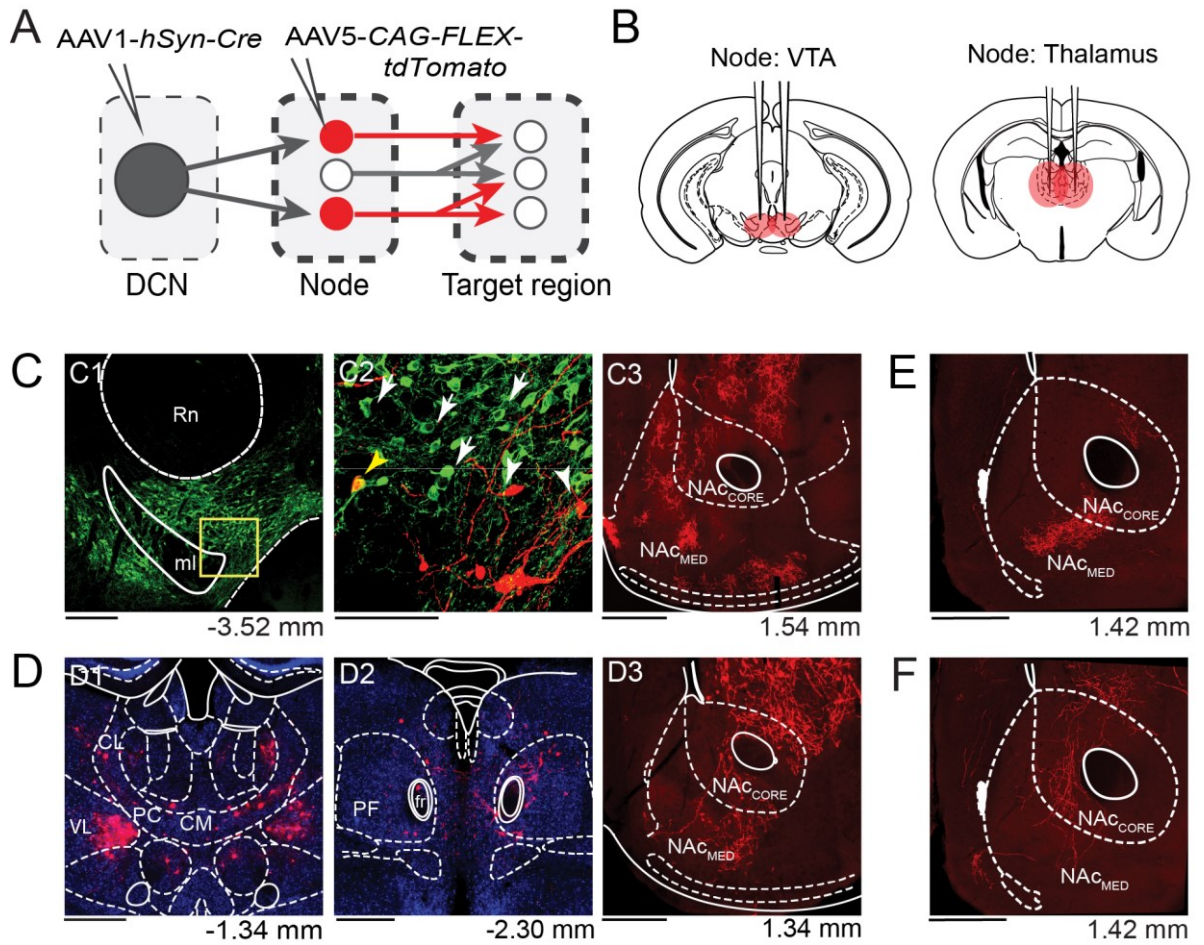

Figure 5. **Disynaptic cerebellum - nucleus accumbens connectivity is confirmed via anterograde transsynaptic viral tracing**. **A**, Schematic diagram of AAV1-mediated transsynaptic labeling approach. **B**, Schematic diagrams of stereotactic injections of floxed fluorophore in VTA and thalamic nodes. **C1**, The VTA is visualized via TH immunostaining (green). Yellow box denotes zoom-in area depicted in C2. Rn: red nucleus; ml: medial lemniscus. **C2**, Neurons that receive DCN input are labeled with tdTomato (red; white arrowheads). Green: TH+ neurons (white arrows). Yellow arrowhead: TH+, tdTomato+ neuron. **C3**, Projections of CB-VTA neurons in NAc_{Core} and NAc_{Med}. **D1**, Neurons that receive DCN input in thalamus are labeled with tdTomato (red). Blue: NeuN. CM: centromedial n.; PC: paracentral n.; CL: centrolateral n.; VL: ventrolateral n. **D2**, Same as D1, but for parafascicular n. (PF). fr: fasciculus retroflexus. **D3**, Projections of CB-thalamic neurons in NAc_{Core} and NAc_{Med}. **E-F**, Fluorescence images from experiments similar to A-B but with only lateral DCN injected with AAV1-Cre. **E**, NAc projections of VTA neurons receiving input from lateral DCN. **F**, Same as in E but for thalamic neurons. Scale bars below images: C1: 200 µm; C2: 100 µm; C3,D1-3,E,F: 500 µm. N = 7 mice. Numbers denote distance from bregma.

the normalized group average excitatory responses of NAc_{Core} and NAc_{Med} neurons elicited by photostimulation in VTA (Fig. 7A1), CM (Fig. 7B1), and PF (Fig. 7C1). Because of jitter, the group average response underestimates the true magnitude of modulation, as discussed previously for electrical responses. Therefore, to further evaluate the connectivity strength in the three CB-NAc circuits, we computed the average peak amplitude of light-evoked excitatory responses in NAc subregions and asked whether it varied across nodes or between NAc subregions. In NAc_{Core}, neurons displayed an average peak excitatory response to photostimulation in VTA of 43 ± 8 spikes/s; in CM: 44 ± 5 spikes/s; in PF: 36 ± 4 spikes/s. In NAc_{Med}, the average peak excitatory response to photostimulation in VTA was 39 ± 6 spikes/s; in CM: 34 ± 3 spikes/s; and in PF: 41 ± 6 spikes/s. There was no statistically significant effect of NAc subregion, or of node, on peak responses (NAc subregion: $F(1,120) = 0.4$; $p = 0.5$; node: $F(2,120) = 0.1$; $p = 0.9$), and no significant interaction ($F(2,120) = 0.9$; $p = 0.4$). These NAc responses were specific to ChR2 expression, as no-opsin (EGFP-alone) controls did not show an effect of photostimulation on peak firing rate, even at 15 mW (response window vs. baseline: NAc_{Core}: $t_4 = 0.53$, $p = 0.62$; NAc_{Med}: $t_{35} = -1.41$, $p = 0.17$) (Fig. 7D).

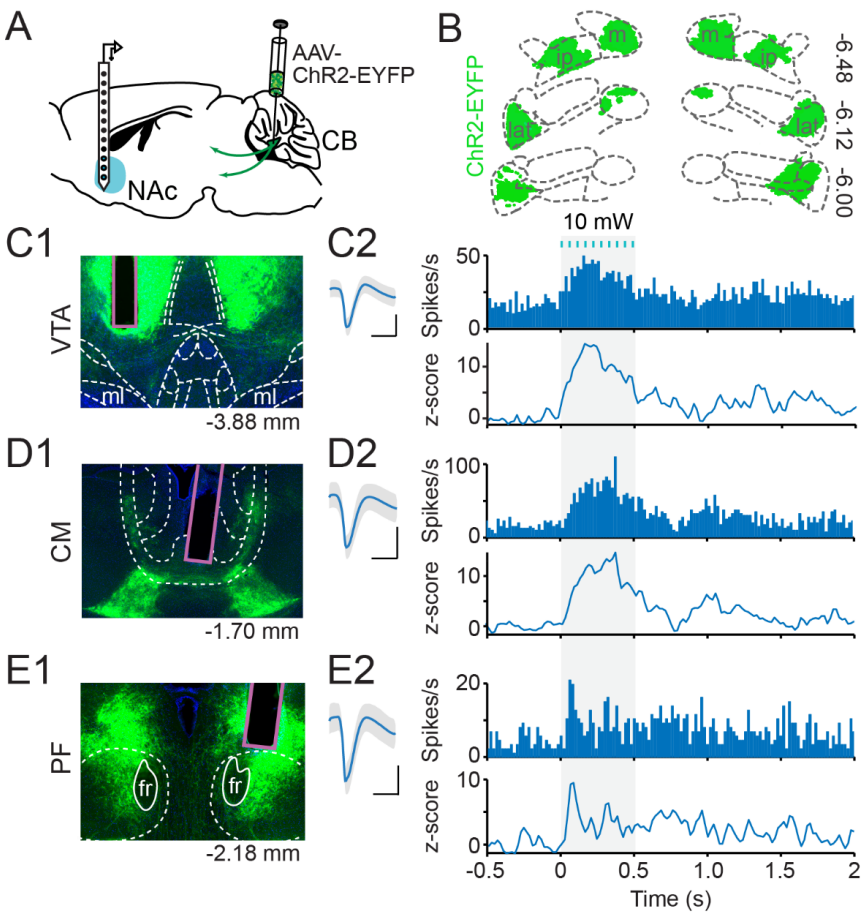

Figure 6. Photostimulation of cerebellar projections in VTA and thalamus elicits responses in nucleus accumbens. A, Schematic diagram of optophysiological approach. *NAc:* nucleus accumbens, *CB:* cerebellum. **B,** Example ChR2-EYFP expression in DCN. lat: lateral n.; ip: interposed n; m: medial n. **C**,**D**,**E**, Histology and NAc responses to optogenetic stimulation of VTA (**C1**,**2**), CM (**D1**,**2**), and PF (**E1**,**2**). **C1**,**D1**,**E1**: Representative images of optic fiber placement. ml: medial lemniscus; fr: fasciculus retroflexus. **C2**,**D2**,**E2**: Example single units. *Left*: Average spike waveform. Scale bars: 1 ms, 10 µV. *Top*: PSTH (10-ms bins) of firing rate (spikes/s). B*ottom*: Baseline-normalized firing rate (z-score) across time. Blue lines denote photostimulation; Shaded area marks response window. Numbers below or next to images indicate distance from bregma (in mm).

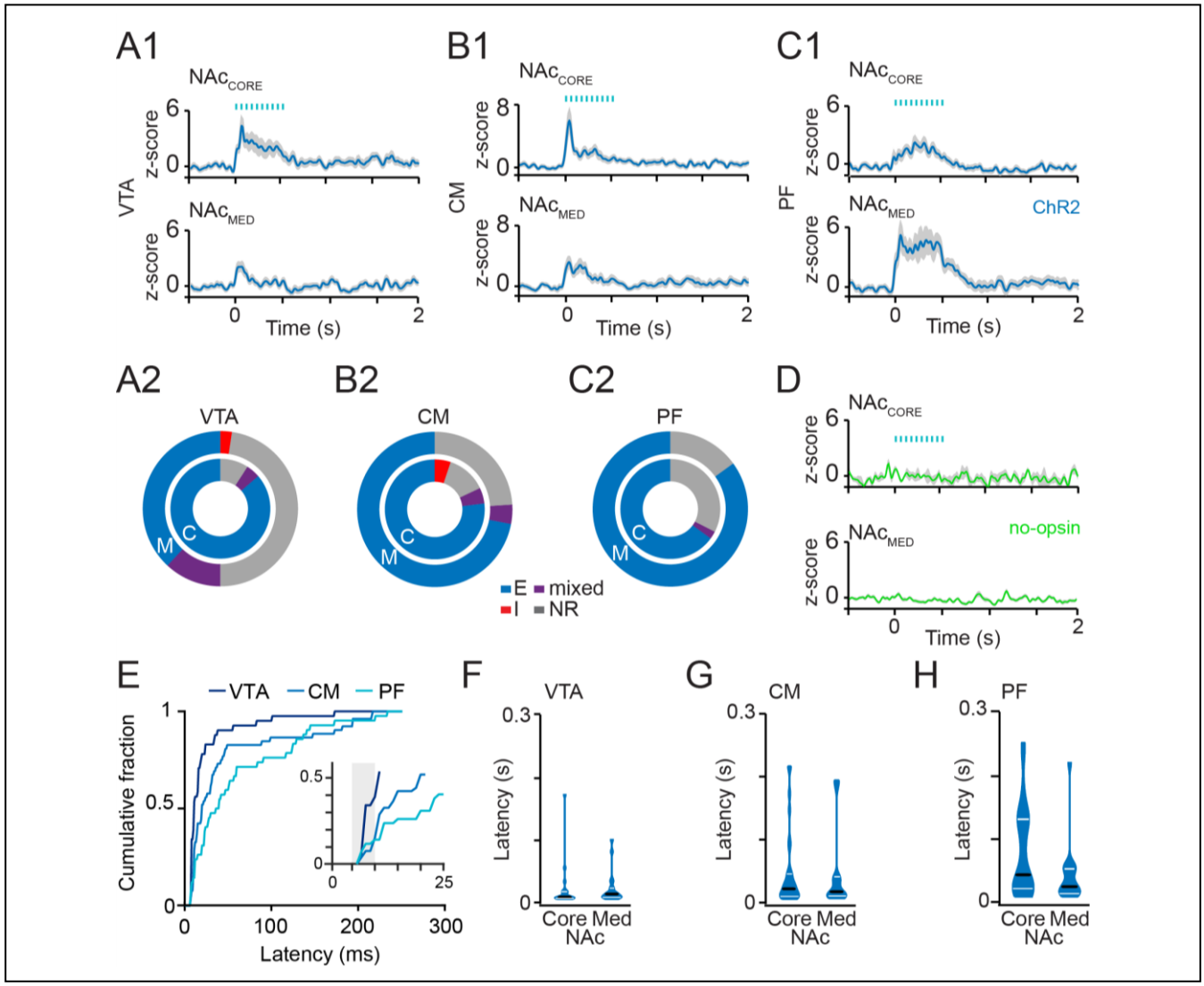

Figure 7. Node-dependent differences in nucleus accumbens responses to photostimulation of cerebellar projections. A1,**B1**,**C1**, Average normalized activity (z-score) in NAc_{Core} (*top*) and NAc_{Med} (*bottom*) as a function of time, for cerebellar fiber photostimulation (blue lines) in VTA (**A1**), CM (**B1**) and PF (**C1**). **A2**,**B2**,**C2**, Distribution of response-types in NAc_{Core} (C: inner ring) and NAc_{Med} (M: outer ring) upon photostimulation of cerebellar projections in VTA (**A2**), CM (**B2**), and PF (**C2**). *Blue:* excitatory (E), *Red*: inhibitory (I), *Purple:* mixed, *Gray:* non-responders (NR). **D**, Average normalized activity (z-score) in NAc_{Core} (*top*) and NAc_{Med} (*bottom*) as a function of time, for no-opsin controls. **E**, Cumulative histogram of NAc response onset latencies upon cerebellar fiber photostimulation in VTA, CM and PF. Inset: 0-25 ms zoom-in. **F**,**G**,**H**, Violin plots of onset latencies of excitatory responses in NAc_{Core} (Core) and NAc_{Med} (Med), upon cerebellar fiber photostimulation in VTA (**F**), CM (**G**) and PF (**H**). Black lines: Median; White lines: interquartile range (Q1-Q3). VTA: N = 4 mice, $n_{NAcCORE}$ = 22 units, n_{NAcMED} = 42 units; CM: N = 4 mice, $n_{NAcCORE}$ = 56 units, n_{NAcMED} = 26 units; PF: N = 3 mice, $n_{NAcCORE}$ = 40 units, n_{NAcMED} = 20 units. D, no-opsin controls: N = 4 mice, $n_{NAcCORE}$ = 5 units, n_{NAcMED} = 36 units.

Light-evoked responses were excitatory in their majority, with frequency distribution that varied between NAc_{Core} and NAc_{Med} in a node-dependent manner: photostimulation of DCN projections in VTA evoked more excitatory responses in NAc_{Core} than in NAc_{Med} (excitatory responses in NAc_{Core}: 86%, in NAc_{Med}: 38%; $\chi^2_{(1)} = 13.6$; $p < 0.001$) (Fig. 7A2), whereas no

256 such differences were observed upon photostimulation in CM (NAc_{Core}: 77%, NAc_{Med}, 72%;
257 $\chi^2_{(1)} = 0.20$; $p = 0.44$) (Fig. 7B2) or PF (excitatory responses in NAc_{Core}: 65%, in NAc_{Med} : 85%;
258 $\chi^2_{(1)} = 2.63$; $p = 0.11$) (Fig. 7C2) (p-values corrected for multiple comparisons). Excitatory
259 responses were also readily elicited in NAc_{Core} and NAc_{Med} with as little as 1 or 5 mW
260 photostimulation (Table 1). Even at the lowest intensity (1 mW), a single pulse was sufficient to
261 elicit a response (percent responses elicited by first pulse in VTA: NAc_{Core}: 54%, NAc_{Med}, 58%;
262 in CM: NAc_{Core}: 72%, NAc_{Med}, 57%; in PF: NAc_{Core}: 67%, NAc_{Med}: 58%) (Table 2), pointing to
263 high-fidelity connectivity that does not strictly require activity-dependent synaptic enhancement
264 to propagate information to NAc. The proportion of responses elicited by the first light pulse
265 tended to increase with photostimulation intensity more than expected by chance alone in VTA
266 (permutation test: $p < 0.001$, $n = 41$, $N = 4$) and CM ($p < 0.01$, $n = 52$, $N = 4$), but not in PF ($p =$
267 0.08, $n = 45$, $N = 3$) (p-values corrected for multiple comparisons). This finding could
268 potentially suggest convergent connectivity within the CB-VTA-NAc and CB-CM-NAc circuits.

		Percent (%) responses					
		VTA		**CM**		**PF**	
Photostimulation Intensity		*NAc Core*	*NAc Med*	*NAc Core*	*NAc Med*	*NAc Core*	*NAc Med*
1 mW	Exc.	59	37	54	41	43	60
	Inh.	5	17	3	6	3	5
	Mixed	0	10	3	0	3	0
	No Res.	36	37	41	53	53	35
	n =	22	41	39	17	40	20
5 mW	Exc.	82	45	54	58	58	75
	Inh.	0	7	13	4	3	0
	Mixed	5	5	5	8	0	15
	No Res.	14	43	29	31	40	10
	n =	22	42	56	26	40	20
10 mW	Exc.	86	38	77	72	65	85
	Inh.	0	2	5	0	0	0
	Mixed	5	12	5	4	3	0
	No Res.	9	48	13	24	33	15
	n =	22	42	39	25	40	20

Table 1. Percent responses in NAc_{Core} and NAc_{Med} elicited by photostimulation of cerebellar axons in VTA, CM and PF at different intensities.

269 In contrast to excitatory responses, inhibitory responses were scarce in photostimulation
270 experiments (Fig. 7A2, B2, C2). This finding appeared to be stimulation regime-dependent,
271 because lowering the photostimulation intensity increased the prevalence of inhibitory

responses in NAc more than expected by chance alone (permutation test, 1 vs. 5 vs. 10 mW: VTA: $p < 0.01$, $n = 64$, $N = 4$; CM: $p < 0.05$, $n = 82$, $N = 4$; PF: $p < 0.05$, $n = 60$, $N = 3$; p-values corrected for multiple comparisons) (Table 1). Finally, we asked whether each NAc subregion was differentially responsive to photostimulation in each of the nodes. We found no differential effect of 10 mW-photostimulation among the three nodes on the distribution of response-types in either NAc_{Core} ($\chi^2_{(2)} = 5.4$; $p = 0.07$) or NAc_{Med} ($\chi^2_{(2)} = 4.9$; $p = 0.09$).

		Proportion of responses elicited by 1st light pulse	
	Photostimulation Intensity	*NAc Core*	*NAc Med*
VTA	1 mW	7/13 (54%)	11/19 (58%)
	5 mW	16/19 (84%)	14/21 (67%)
	10 mW	18/20 (90%)	19/21 (90%)
CM	1 mW	16/22 (72%)	4/7 (57%)
	5 mW	27/33 (82%)	14/17 (82%)
	10 mW	26/32 (81%)	16/19 (84%)
PF	1 mW	12/18 (67%)	7/12 (58%)
	5 mW	15/23 (65%)	16/18 (89%)
	10 mW	14/27 (52%)	14/17 (82%)

Table 2. Proportion of excitatory responses in NAc_{Core} and NAc_{Med} elicited by the first light pulse, at different photostimulation intensities.

Temporal aspects of light-evoked responses

We wondered whether temporal aspects of CB-NAc communication differed between excitatory and inhibitory responses. This question cannot be addressed accurately in electrical stimulation experiments because of electrical artifacts, which can place a lower bound on the onset latency of detected responses, but can be readily addressed in optogenetic experiments. Analysis of onset latency of responses elicited by 10 mW CB axonal photostimulation indicated that, overall, excitatory responses had significantly shorter onset latencies than inhibitory ones (mean ± sem: excit.: 45.4 ± 5.0 ms, inh.: 256.7 ± 46.2 ms, $t_{147} = -10.0$, $p < 0.001$; $N = 10$, $n_{exc.} = 136$, $n_{inh.} = 13$). To dissect node-specific effects, we computed the cumulative distributions of onset latencies for excitatory responses elicited by photostimulation in VTA, CM and PF (Fig. 7E). A relatively broad distribution of onset latencies was evident in all nodes, with half-rise latencies of 11 ms for VTA, 20 ms for CM and 40 ms for PF. Further analysis indicated that the

290 probability of eliciting short-latency responses (≤ 10 ms), which are consistent with disynaptic
291 connectivity (Chen et al., 2014; Gao et al., 2018; Assous et al., 2019; Yang et al., 2021), was
292 greater for photostimulation in VTA compared to CM and/or PF (proportion of latencies ≤ 10
293 ms: VTA: 0.34, CM: 0.08, PF: 0.11; VTA vs CM: $\chi^2_{(1)} = 10.3$, $p < 0.01$; VTA vs PF: $\chi^2_{(1)} = 6.4$, p
294 < 0.01; CM vs PF: $\chi^2_{(1)} = 0.4$, $p = 0.54$; p-values corrected for multiple comparisons) (Fig. 7E
295 *inset*). Similar analysis could not be applied to inhibitory responses because of their limited
296 prevalence (Fig. 7A2-C2 and Table 1). Finally, we examined NAc subregion-specific effects on
297 excitatory response latencies (Fig. 7F-H). A two-way ANOVA corroborated the significant main
298 effect of nodes ($F(2,130) = 4.7$; $p < 0.05$) but did not find significant main effect of NAc
299 subregion ($F(1,130) = 1.7$; $p = 0.19$), or significant interaction effect between node and NAc
300 subregion ($F(2,130) = 1.7$; $p = 0.18$).

301 Collectively, these results support and expand the conclusions of our neuroanatomical
302 and electrical microstimulation studies that signals originating in DCN can reach NAc through
303 pathways that involve the VTA and the intralaminar thalamus.

304 Discussion

305 In this study we examined the previously uncharted functional connectivity between the
306 cerebellum and nucleus accumbens using in vivo electrophysiology, neuroanatomy, and
307 optogenetics. We found that electrical microstimulation of DCN elicits responses in both
308 NAc_{Core} and NAc_{Med}, manifested as excitatory and/or inhibitory modulations of neural firing
309 rate. Neuroanatomical studies identified three disynaptic pathways through which cerebellar
310 signals can reach the NAc. These pathways go through the VTA or the intralaminar thalamus
311 (centromedial or parafascicular nucleus). Optogenetic activation of DCN axons in each of
312 these intermediary nodes revealed that all three pathways can communicate cerebellar signals
313 to NAc, albeit with distinct node-dependent properties.

314 Bidirectional regulation of NAc through fast excitation and slow inhibition

315 Results from both electrical microstimulation and optogenetic experiments converged on
316 the conclusion that the cerebellum sends strong excitatory signals to NAc. The strength of
317 these excitatory signals did not show any NAc subregion-, or node-, dependence. However,
318 the relative frequency of NAc neurons that receive excitatory vs. inhibitory (or mixed) signals

319 varied, depending on the route that the DCN signals followed: the CB-VTA pathway was more
320 likely to communicate excitatory signals to neurons in NAc_{Core} than in NAc_{Med}, whereas the CB-
321 thalamic pathways did not show a clear preference for either NAc subregion.

322 Our neuroanatomical studies identified three disynaptic pathways for CB-NAc
323 communication through the VTA and intralaminar thalamus (CM, PF) nodes. Disynaptic
324 pathways that utilize fast classical neurotransmitters (e.g., glutamate) would be expected to
325 support rapid signal propagation and result in short-latency responses, whereas
326 neuromodulatory (e.g., dopaminergic) pathways would be expected to operate at longer time
327 scales (Chen et al., 2014; Gao et al., 2018; Assous et al., 2019; Liu et al., 2021; Yang et al.,
328 2021; Sippy and Tritsch, 2023). The shortest-latency responses we recorded upon
329 photostimulation of cerebellar axons in each of the intermediary nodes occurred within 10 ms,
330 a finding that is consistent with the monosynaptic connections known to exist between DCN
331 and VTA, and DCN and thalamus (Carta et al., 2019; Baek et al., 2022; Jung et al., 2022), and
332 which agrees with our newly identified structural connectivity. Particularly for responses elicited
333 by photostimulation in VTA, DCN axons are known to synapse onto both dopaminergic and
334 non-dopaminergic VTA neurons (Beier et al., 2019; Carta et al., 2019; Baek et al., 2022),
335 including vesicular glutamate transporter 2-positive (vGlut2+) VTA neurons, which project to
336 NAc (Beier et al., 2015) and which could, at least partly, mediate cerebellar signaling. Longer-
337 latency excitatory responses dominate CB-NAc communication through the intralaminar
338 thalamus and could arise from polysynaptic circuitry, in agreement with the diffuse patterning
339 of intralaminar projections (Jones and Leavitt, 1974; Van der Werf et al., 2002). Subthreshold
340 synaptic signaling that requires activity-dependent short-term facilitation in order to propagate
341 to NAc neurons could also account for longer latencies. Given that optogenetic stimulation of
342 CB axons with a single pulse could elicit NAc responses, short-term plasticity does not appear
343 to be strictly required for successful CB-NAc communication. However, it could account for the
344 excitatory NAc responses evoked through PF, which displayed more gradual buildup than
345 excitatory responses through the other nodes.

346 Inhibitory responses are also a key component of CB-NAc connectivity and may be
347 important for global gain control (Buzsáki et al., 2007). Inhibitory responses (and/or inhibitory
348 components of mixed responses) were seen upon stimulation in DCN, or in any of the nodes,
349 and occurred with longer latencies compared to excitatory responses. They also appeared to

depend on photostimulation intensity, with higher prevalence at lower photostimulation intensities. Multiple cellular mechanisms could underlie inhibitory responses and could involve dopamine release as well as non-dopaminergic signaling through the VTA (Brown et al., 2012; Beier et al., 2019; Carta et al., 2019; Baek et al., 2022) and/or CB-thalamic (CM, PF) projections to NAc, which are known to contact not only medium spiny neurons but also cholinergic inhibitory interneurons (Yamanaka et al., 2018). Polysynaptic pathways could also be involved, although their recruitment seems at odds with the inverse relationship between inhibitory response prevalence and photostimulation intensity. The nature of synaptic signaling and plasticity in CB-NAc circuits is an exciting route for further investigation.

Technical considerations

Our recordings were performed in ketamine-anesthetized mice. Although ketamine at anesthetic doses does not alter the number of spontaneously active striatal neurons (Kelland et al., 1991), it affects the pattern of spontaneous activity, promoting step-like membrane potential fluctuations between “up-” and “down-states” (Mahon, 2001). Such bursting behavior would contribute to “noisy” baseline activity; however, we would not expect it to distort our analyses because we have defined neural responses as changes in spiking rate from the preceding baseline. Moreover, by using electrical and/or optogenetic, rather than sensory, stimuli to probe connectivity, we have overcome any concerns stemming from the known inhibitory effect of ketamine on sensory-evoked activity in the cerebellum (Bengtsson and Jörntell, 2007).

In addition to anesthesia, the stimulation modality (electrical, optogenetic) warrants consideration. Electrical stimulation could potentially result in antidromic activation of DCN inputs, which could lead to recruitment of alternate polysynaptic pathways to NAc. This concern was mitigated by our optogenetic experiments, in which ChR2-expessing DCN axons were specifically activated in the nodes. Moreover, although electrical current propagates widely in the brain, the use of bipolar electrodes allowed us to restrict the spread of DCN stimulation to ~100 μm, as shown by the substantial drop in the probability to activate the same NAc neuron with DCN stimuli delivered 100 μm apart. Lastly, optogenetic stimulation of DCN axons in a node could induce back-propagating action potentials that could, in turn, elicit NAc responses through axonal collaterals. However, to the best of our knowledge, there is no

evidence for DCN collaterals that form synapses onto NAc-projecting neurons in both VTA and intralaminar thalamic nuclei. Even if such collaterals existed, their activation would result in unreliable responses with relatively long latencies, due to synaptic delays and the failure-prone asymmetric nature of action potential conduction velocity (Grill et al., 2008; Mateus et al., 2021).

Novelty of anatomical connections

Anatomical and functional connections between DCN and VTA, and DCN and intralaminar nucleus nodes, have been described previously (Snider and Maiti, 1976; Hendry et al., 1979; Phillipson, 1979; Watabe-Uchida et al., 2012; Gornati et al., 2018; Carta et al., 2019; Jung et al., 2022). VTA and thalamic projections to NAc are also well established (Beckstead et al., 1979; Su and Bentivoglio, 1990; Bentivoglio et al., 1991; Bassareo and Di Chiara, 1999; Garris et al., 1999; Groenewegen et al., 1999; Van der Werf et al., 2002; Ikemoto, 2007; Taylor et al., 2014). It might therefore be unsurprising that the DCN recruit these nodes to communicate with NAc. However, the VTA and thalamus are exquisitely complex areas with multiple output streams. For example, the VTA projects not only to NAc but also to hippocampus, hypothalamus, lateral habenula, entorhinal cortex, etc. (Oades and Halliday, 1987; Stamatakis et al., 2013; Beier et al., 2015). None of these downstream target regions appears to be disynaptically connected to DCN through the VTA, which points to specificity in circuit wiring. Our study is the first one, to our knowledge, to map DCN-NAc circuits through VTA and thalamus. A recent study provided anatomical evidence for a medial DCN-NAc circuit (Fujita et al., 2020). Here we extend these observations to lateral DCN and also provide evidence for the centromedial and parafascicular nuclei as parts of the thalamic node.

Ideas and Speculations

It is tempting to speculate on network-wide implications of the different CB-NAc pathways. Fast excitatory signals would be well poised to support the rapid communication of information critical to the control of motivated behavior, such as prediction or prediction-error signals, which are well established in the cerebellum (Wagner et al., 2017; Heffley and Hull, 2019; Kostadinov et al., 2019; Larry et al., 2019). The fact that DCN signals can reach NAc_{Core}

409 and NAc_{Med} through distinct anatomical (and possibly cellular) pathways leaves room for
410 distinct multiplexing with signals originating elsewhere.

411 Cerebellar signals that arrive to NAc_{Core} through VTA could be behaviorally relevant for
412 reward learning through signaling of value, which has been correlated with dopamine release
413 in NAc_{Core}, but not in NAc_{Med} (Mohebi et al., 2019). Alternatively (or additionally), the CB-VTA-
414 NAc_{Core} pathway could be rewarding in itself, as stimulation of dopaminergic projections from
415 VTA to NAc_{Core} are sufficient to establish self-stimulation (Han et al., 2017) and previous
416 studies have shown that the CB can signal reward (Wagner et al., 2017; Carta et al., 2019;
417 Medina, 2019). The CB-VTA-NAc_{Core} pathway could also be involved in social cognition, given
418 that NAc_{Core} activation promotes social dominance in mice and that cerebellar Purkinje neurons
419 are known to modulate social aggression in mice (Jackman et al., 2020). Finally, the CB-VTA-
420 NAc_{Core} pathway could also be important for signaling salience, regardless of valence, to
421 promote learned responses to behaviorally relevant stimuli (Kutlu et al., 2021). The short
422 response latencies of the CB-VTA-NAc_{Core} pathway could be key for temporally precise control
423 of behavioral states including attentional control (Flores-Dourojeanni et al., 2021), and could
424 gate incoming signals to NAc, including signals from PF (Akaike et al., 1981; Hara et al.,
425 1989).

426 The observed bias of CB-PF neurons to preferentially influence NAc_{Med} over NAc_{Core} could
427 support a role in behavioral flexibility. Indeed, both NAc_{Med} and NAc_{Core} neurons encode
428 rewarding and aversive stimuli via changes in neural firing rate, however, only neurons in
429 NAc_{Med} adaptively shift population response type to track the motivational value of a stimulus
430 (Loriaux et al., 2011), suggesting that NAc_{Med} can flexibly modulate encoding based on relative
431 stimulus valence and/or acquired salience (Aquili et al., 2014; West and Carelli, 2016). Given
432 that the PF is known to play a role in behavioral flexibility (Brown et al., 2010; Kato et al.,
433 2021), the CB-PF-NAc_{Med} circuit may communicate teaching signals for updating past learning
434 and altering behavior adaptively.

435 Future investigations into the cellular basis of DCN-NAc communication as well as
436 potential circuit-specificity of behavioral contributions are clearly in order. Here, we have
437 broken new ground by providing the first evidence of rapid functional connectivity between CB
438 and NAc, through the midbrain and intralaminar thalamus.

439 **Materials and Methods**

440 **In vivo electrophysiology**

441 **Mice**

442 C57Bl/6J mice of both sexes were used in accordance with the National Institutes of
443 Health guidelines and the policies of the University of California Davis Committee for Animal
444 Care. Acute in vivo recordings were performed at postnatal days P43-P91. All animals were
445 maintained on a light/dark cycle (light 7 am - 7 pm), and experiments were performed during
446 the light cycle.

447 **Surgery**

448 Mice of both sexes (P35 - P49; N = 11) were used for optogenetic experiments.
449 Animals were anesthetized with isoflurane (4% - 5% induction; 1.5% maintenance) and
450 secured to a stereotactic frame (Kopf Insruments, Tujunga, CA). After exposing the top of the
451 skull, the head was leveled and small craniotomies were drilled over the DCN.
452 Channelrhodopsin-expressing adeno-associated virus (AAV2-hSyn-hChR2(H134R)-EYFP,
453 UNC Vector Core, Chapel Hill, NC; 100 nl, $5.6x10^{12}$ gc/ml, 1:2 dilution) was injected into the
454 three DCN using a Micro4 controller and UltraMicroPump 3 (VWR, Radnor, PA). Glass
455 needles were made from 1-mm outer diameter glass pipettes (Wiretrol II, Drummond Scientific
456 Company, Broomall, PA) pulled to a fine tip (20 - 50 µm tip diameter, 3 - 4 mm tip length) using
457 a pipette puller (P-97, Sutter Instrument, Novato, CA). Injection needles were left in place for 5-
458 10 min following injections to minimize diffusion. The following coordinates were used for
459 targeting pipettes to each nucleus (relative to lambda): medial n.: -2.55 AP, +/-0.8 ML, -2.15
460 DV; interposed n.: -2.45 AP, +/-1.7 ML, -2.15 DV; lateral n.: -1.82 AP, +/- 2.37 ML, -2.17 DV.
461 Following surgery and analgesia administration (0.1 mg/kg buprenorphine, 5 mg/kg
462 meloxicam), mice were allowed to recover on a warm heating pad before being transferred
463 back to the vivarium. Animals were given 4-5 weeks expression time before being used in in
464 vivo recording experiments.

465 For electrophysiological recordings, anesthesia was initially induced by brief inhalation
466 of 4-5% isoflurane followed by an intraperitoneal injection of anesthetic cocktail (100 mg/kg
467 ketamine; 10 mg/kg xylazine; 1 mg/kg acepromazine) and was maintained with periodic

468 injections of the anesthetic cocktail (20-50 mg/kg), as needed. After confirmation of anesthesia
469 depth using a toe pinch response test, mice were placed in a stereotactic frame (Stoelting Co.,
470 Wood Dale, IL) on a heating pad. Breathing rate and toe pinch responses were monitored to
471 ensure maintenance of anesthesia. For electrical stimulation experiments (N = 42 mice of both
472 sexes), a small craniotomy and durectomy were performed over the DCN (lateral/interposed
473 n.: relative to lambda, in mm: -2.1 to -2.6 AP; +/-2.1 to +/-2.3 ML). For optogenetic
474 experiments, optic fibers were implanted over the CM (relative to bregma: -1.3 AP; -.85 ML; -
475 3.55 DV, 10° angle), PF (relative to bregma: -1.87 AP; -.95 ML; -2.95 DV, 12° angle), or VTA
476 (relative to bregma: -3.1 AP; -0.5 ML; -4.05 DV) ipsilaterally to recording site and secured with
477 temporary resin acrylic (Keystone Industries, Gibbstown, NJ). For recordings, craniotomy and
478 durectomy were made over NAc, targeting the medial shell and/or core (relative to bregma:
479 +1.7 to +1.54 AP; +/- 0.4 to +/-1.15 ML).

480 **Electrical/Optical Stimulation**

481 For electrical stimulation, a custom stereotrode (~200 μm distance between tips) was
482 lowered 1.95 - 2.45 mm below the brain surface (in DV axis) through the cerebellar craniotomy
483 to reach the DCN. Ten trials of bipolar constant-current electrical microstimulation were
484 delivered at each location at a 15-s inter-trial interval. Each stimulation trial consisted of a 200-
485 Hz burst of five 0.5-ms monophasic square-waveform pulses at 100 μA. In a subset of
486 experiments (N = 15 mice), the stimulation intensity was varied between 30, 100, and 300 μA
487 in interleaved blocks of 5 trials per intensity. When stimulation was repeated at different DCN
488 sites in the same experiment, an effort was made to move the stereotrode in a direction
489 perpendicular to the axis of the two poles, so that an at least partly distinct pool of cerebellar
490 neurons could be stimulated. For optical stimulation, 20-50 trials of ten 5-ms light pulses (473-
491 nm DPSS laser, Opto Engine LLC, Midvale, UT) were delivered at 20 Hz (inter-trial interval: 30
492 s or 1 min). Optical stimulation was primarily delivered at 10 mW intensity at fiber tip, but lower
493 intensities were also tested (1 and 5 mW).

494 **Acquisition of Electrophysiological Data**

495 Recordings were performed with a 12-channel (platinum; 0.2 - 2 MΩ impedance) axial
496 multi-electrode array (FHC Inc., Bowdoin, ME; 150 μm distance between channels), dipped in

497 fluorescein dextran (3000 MW) and lowered into the NAc at a depth of 3.75 - 5.25 mm below
498 the brain surface (DV axis). Electrode signals were fed to a digital headstage (RHD 2132, Intan
499 Technologies, Los Angeles, CA) for amplification (x20), filtering (0.7 - 7500 Hz) and digitization
500 (30 kS/s with 16-bit resolution), before transfer to an open-source acquisition system
501 (OpenEphys) for display and storage.

502 **Histology for Verification of Electrode/Optic Fiber Placement**

503 Positioning of electrodes and fibers was initially guided by atlas-based stereotactic
504 coordinates (Paxinos & Franklin) and, upon completion of experiments, histologically verified
505 through electrolytic lesions (for location of DCN microstimulation electrodes; single 10-s
506 cathodal pulse of 300 μA), fiber track inspection (for optic fiber) and fluorescence imaging (for
507 recording array; NAc fluorescein dye track). Coordinates for subsequent animals of the same
508 litter were further adjusted accordingly. At the end of experiments, electrodes were retracted
509 and animals were perfused with 4% (w/v) paraformaldehyde (PFA) in 0.1 M phosphate buffer
510 (PB). Brains were dissected and post-fixed in 4% PFA, sliced in phosphate buffered saline
511 (PBS) and inspected under a fluorescence stereoscope (Olympus, Tokyo, Japan; SZX2). NAc
512 slices containing the dye track from the recording array were identified under 488 nm light; CB
513 slices with electrolytically lesioned tissue, and thalamic and/or VTA slices with optic fiber tracts,
514 were identified under brightfield illumination. Slices of interest were subsequently stained with
515 DAPI (1:20,000, Thermo Fisher Scientific Inc., Waltham, MA), mounted on slides, and imaged
516 using a VS120 Olympus slide scanner. Images were manually registered to the Paxinos and
517 Franklin Mouse Brain Atlas and the location of the recording electrode tip and optic fiber were
518 mapped. Only channels along the recording array that were determined to be within NAc_{Core}
519 and/or NAc_{Med} were included in analysis. Experiments with misplaced optic fibers, viral
520 expression outside the DCN region, or cerebellar electrolytic lesions localized outside the
521 lateral and/or interposed DCN, were excluded from analysis.

522 **Quantification and Statistical Analysis**

523 **Electrophysiological data processing and quantification**

524 Custom-written MATLAB scripts (Mathworks, Natick, MA) were used for data
525 processing and analysis. Filtering of spikes was achieved through a 4th-order Butterworth high-

pass filter (cutoff at 300 Hz). The filtered signal was thresholded at 3-3.5 standard deviations below the average voltage. Spikes were subsequently sorted in putative single-unit clusters with Plexon Offline Sorter (version 3.3.5, Plexon Inc., Dallas, TX) using principal component analysis. All well-isolated neurons were included in the analyses. Firing rates were computed from spike counts in consecutive 10-ms time bins (peri-stimulus time histogram; PSTH). Spikes with time differences less than 7 ms from stimulus artifacts or 1 ms from the previous spike were discarded.

Quantification of stimulation-induced modulation of NAc spiking activity followed recent studies of cerebellar neurons (Chen et al., 2014; Washburn et al., 2022) and our own evaluation of the dataset. Specifically, we averaged the PSTH across all trials of the same intensity for any given pair of recording and stimulation sites and normalized to the average pre-stimulus baseline (z-score). We defined an excitatory response as an increase in firing rate that exceeded 3 standard deviations (σ) above the baseline within the first 500 ms after the stimulus onset. An inhibitory response was defined as a decrease in firing rate of more than 1 σ below the baseline that persisted for a minimum of three time bins (i.e., 30 ms) and started within the first 500 ms after stimulus onset. The 500-ms time window captured more than 90% of responses (not shown). For single-unit responses that included both excitatory and inhibitory components (mixed responses), we quantified each component individually for amplitude and latency. For illustration purposes only, all firing rates were convolved with a Gaussian kernel (σ = 16 ms). Response onset latency was defined as the first instance at which firing rate changed from baseline as described above, using 1-ms time bins. For analyses of multi-unit activity, see our BioRxiv preprint (D'Ambra et al., 2020).

Statistics

Statistical analyses were performed in Graphpad Prism 9.3.0 and Matlab. Comparisons of the relative frequency distribution of response types were performed with Contingency Table analyses (Chi-square tests). Comparisons of response latencies and firing rates were performed with t-tests and ANOVA. For permutation tests, we randomly shuffled the data between groups 1,000 times and estimated the probability to find a difference greater than or equal to the observed difference by chance alone (Oden and Wedel, 1975; Antzoulatos and

555 Miller, 2011). To correct for multiple comparisons, we followed the Benjamini-Hochberg
556 method (Benjamini and Hochberg, 1995) with False Discovery Rate (FDR) set at 10%.

557 **Surgery for anatomical studies**

558 For anatomical tracing, juvenile mice of both sexes were injected with AAVs and tracers
559 using the procedure described above for in vivo optophysiology. For co-localization
560 experiments: AAV9-CAG-GFP (2 x 10^{12} viral particles/ml, UNC viral core) was injected in DCN
561 (from bregma, in mm: medial n.: -2.55 AP, ± 0.75 ML, -2.1 DV, 50 nl; interposed n. : -2.5 AP, ±
562 1.55 ML, -2.1 DV, 50 nl; lateral n.: -2.2 AP, ± 2.3 ML, -2.12 DV, 50 nl; and -1.8, ± 2.35 ML, -
563 2.12 DV, 50 nl). Cholera toxin subunit B (ctb)- 640 or -568 (5 mg/ml, Biotium) was injected in
564 NAc medial shell and core (from bregma, in mm: 1.8 AP, ± 0.8 ML, -4.2 DV, 200 nl). For
565 anterograde transsynaptic tracing: AAV1-hSyn-Cre-WPRE-hGH (10^{13} gc/ml, Addgene; 1:10
566 dilution) was injected in DCN (coordinates as above). AAV5-CAG-FLEX-tdTomato (7.8 x 10^{12}
567 viral particles/ml, UNC viral core; 1:2 dilution) or AAV5-pCAG-FLEX-EGFP-WPRE (1.1 x 10^{13}
568 gc/ml, Addgene; 1:2 dilution) was injected in VTA (from bregma, in mm: 2.8 AP, ± 0.35 ML, -
569 4.2 DV, 100 nl; and -2.85 AP, ± 0.6 ML, -4.2 DV, 100 nl) or thalamus (from bregma, in mm: -
570 0.85 AP, ± 0.3 ML, -3.3 DV, 300 nl; and -1.2 AP, ± 0.5 ML, -3.5 DV, 300 nl; 1:5 dilution).
571 Following surgery, mice remained in the colony for 2-3 weeks to allow for recovery and
572 retrograde labeling/virus expression prior to euthanasia and tissue collection/processing.

573 **Histology and fluorescence microscopy for anatomical studies**

574 Two to three weeks following tracer/virus injections, mice were anesthetized with the
575 anesthetic cocktail and perfused transcardially with 4% (w/v) PFA in PB. Brains were post-
576 fixed in 4% PFA for 6 h and transferred to 30% sucrose in PBS for overnight incubation at 4°C.
577 Brains were coronally sectioned (60 µm) on a sliding microtome, stained with DAPI, mounted
578 to slides, coverslipped with Mowiol-based antifade solution and imaged. VTA sections were
579 immunostained for tyrosine hydroxylase (TH) prior to mounting, as follows: slices were first
580 incubated with blocking solution [10% normal goat serum (NGS) in PBS supplemented with
581 0.3% Triton-X100; PBST] for 1 h at room temperature, then with mouse anti-TH (clone LNC11,
582 Millipore Sigma, Burlington, MA; 1:1000) in blocking solution with 2% NGS overnight at 4°C.
583 Sections were washed with PBST (3 x 20 min) and incubated for 1 h at room temperature with

584 goat anti-mouse Alexa fluor 488 secondary antibody (1:1000), washed with PBS (3 x 20 min),
585 mounted, coverslipped and imaged. Epifluorescence image mosaics were acquired on an
586 Olympus VS120 slide scanner with a 10x air objective. High magnification confocal images
587 were taken sequentially with different laser lines and a 63x oil-immersion objective on a Zeiss
588 LSM800 microscope with Airyscan. Image brightness/contrast was adjusted using ImageJ
589 (NIH) for display purposes. Data from a total of N = 13 mice with successful injections, without
590 spill to neighboring regions, are presented.

591 **Acknowledgments**: We thank Amber Arif and Alicia Dye for help with tissue sectioning; Drs.
592 Brian Wiltgen, Karen Zito, Marty Usrey and Brian Mulloney of UC Davis for access to
593 equipment; Dr. Ditterich for comments on a previous version of the manuscript; and Dr.
594 Chaudhuri for helpful discussions. Author contribution: AD, EA and DF designed the research;
595 AD, SJJ and KV performed the research; AD, KV and EA analyzed the data; SG assisted with
596 tissue slicing and registration; SJJ prepared the anatomy figures; AD, EA and DF wrote the
597 paper with feedback from all authors. This work was supported by a Whitehall fellowship,
598 BRFSG-2017-02, R21MH114178, NSF1754831 and R01MH128744 to DF; a NARSAD 2018
599 Young Investigator Grant to EA; AD was supported by NIH T32 GM007377 and a UC Davis
600 Dean's Distinguished Graduate Fellowship; KV was supported by NIMH T32 MH112507 and
601 F31MH131405 by NIMH.

602 **Competing interests**

603 The authors declare that the research was conducted in the absence of any commercial or
604 financial relationships that could be construed as a potential conflict of interest.
605

References

Adamaszek M, D'Agata F, Ferrucci R, Habas C, Keulen S, Kirkby KC, Leggio M, Mariën P, Molinari M, Moulton E, Orsi L, Van Overwalle F, Papadelis C, Priori A, Sacchetti B, Schutter DJ, Styliadis C, Verhoeven J (2017) Consensus Paper: Cerebellum and Emotion. The Cerebellum 16:552–576.

Akaike A, Sasa M, Takaori S (1981) Inhibition from ventral tegmental area of nucleus accumbens neurons in the rat. Brain Research 225:189–194.

Albert TJ, Dempesy CW, Sorenson CA (1985) Anterior cerebellar vermal stimulation: Effect on behavior and basal forebrain neurochemistry in rat. Biological Psychiatry 20:1267–1276.

Antzoulatos EG, Miller EK (2011) Differences between Neural Activity in Prefrontal Cortex and Striatum during Learning of Novel Abstract Categories. Neuron 71:243–249.

Aquili L, Liu AW, Shindou M, Shindou T, Wickens JR (2014) Behavioral flexibility is increased by optogenetic inhibition of neurons in the nucleus accumbens shell during specific time segments. Learn Mem 21:223–231.

Assous M, Dautan D, Tepper JM, Mena-Segovia J (2019) Pedunculopontine Glutamatergic Neurons Provide a Novel Source of Feedforward Inhibition in the Striatum by Selectively Targeting Interneurons. J Neurosci 39:4727–4737.

Badrinarayan A, Wescott SA, Vander Weele CM, Saunders BT, Couturier BE, Maren S, Aragona BJ (2012) Aversive Stimuli Differentially Modulate Real-Time Dopamine Transmission Dynamics within the Nucleus Accumbens Core and Shell. Journal of Neuroscience 32:15779–15790.

Baek SJ, Park JS, Kim J, Yamamoto Y, Tanaka-Yamamoto K (2022) VTA-projecting cerebellar neurons mediate stress-dependent depression-like behaviors. eLife 11:e72981.

Bassareo V, Di Chiara G (1999) Differential responsiveness of dopamine transmission to food-stimuli in nucleus accumbens shell/core compartments. Neuroscience 89:637–641.

Bauer DJ, Kerr AL, Swain RA (2011) Cerebellar dentate nuclei lesions reduce motivation in appetitive operant conditioning and open field exploration. Neurobiology of Learning and Memory 95:166–175.

Beckstead RM, Domesick VB, Nauta WJH (1979) Efferent connections of the substantia nigra and ventral tegmental area in the rat. Brain Research 175:191–217.

Beier KT, Gao XJ, Xie S, DeLoach KE, Malenka RC, Luo L (2019) Topological Organization of Ventral Tegmental Area Connectivity Revealed by Viral-Genetic Dissection of Input-Output Relations. Cell Rep 26:159-167.e6.

639 Beier KT, Steinberg EE, DeLoach KE, Xie S, Miyamichi K, Schwarz L, Gao XJ, Kremer EJ,
640 Malenka RC, Luo L (2015) Circuit Architecture of VTA Dopamine Neurons Revealed by
641 Systematic Input-Output Mapping. Cell 162:622–634.

642 Bengtsson F, Jörntell H (2007) Ketamine and Xylazine Depress Sensory-Evoked Parallel Fiber
643 and Climbing Fiber Responses. Journal of Neurophysiology 98:1697–1705.

644 Benjamini Y, Hochberg Y (1995) Controlling the False Discovery Rate: A Practical and
645 Powerful Approach to Multiple Testing. Journal of the Royal Statistical Society: Series B
646 (Methodological) 57:289–300.

647 Bentivoglio M, Balercia G, Kruger L (1991) Chapter 4 The specificity of the nonspecific
648 thalamus: The midline nuclei. In: Progress in Brain Research, pp 53–80. Elsevier.
649 Available at: https://linkinghub.elsevier.com/retrieve/pii/S0079612308630472.

650 Brady RO, Gonsalvez I, Lee I, Öngür D, Seidman LJ, Schmahmann JD, Eack SM, Keshavan
651 MS, Pascual-Leone A, Halko MA (2019) Cerebellar-Prefrontal Network Connectivity and
652 Negative Symptoms in Schizophrenia. American Journal of Psychiatry 176:512–520.

653 Brown HD, Baker PM, Ragozzino ME (2010) The Parafascicular Thalamic Nucleus
654 Concomitantly Influences Behavioral Flexibility and Dorsomedial Striatal Acetylcholine
655 Output in Rats. Journal of Neuroscience 30:14390–14398.

656 Brown MTC, Tan KR, O'Connor EC, Nikonenko I, Muller D, Lüscher C (2012) Ventral
657 tegmental area GABA projections pause accumbal cholinergic interneurons to enhance
658 associative learning. Nature 492:452–456.

659 Buckner RL (2013) The cerebellum and cognitive function: 25 years of insight from anatomy
660 and neuroimaging. Neuron 80:807–815.

661 Buzsáki G, Kaila K, Raichle M (2007) Inhibition and Brain Work. Neuron 56:771–783.

662 Carta I, Chen CH, Schott AL, Dorizan S, Khodakhah K (2019) Cerebellar modulation of the
663 reward circuitry and social behavior. Science 363:eaav0581.

664 Caston J, Chianale C, Delhaye-Bouchaud N, Mariani J (1998) Role of the cerebellum in
665 exploration behavior. Brain Res 808:232–237.

666 Chen CH, Fremont R, Arteaga-Bracho EE, Khodakhah K (2014) Short latency cerebellar
667 modulation of the basal ganglia. Nature Neuroscience 17:1767–1775.

668 Corbit LH, Balleine BW (2011) The General and Outcome-Specific Forms of Pavlovian-
669 Instrumental Transfer Are Differentially Mediated by the Nucleus Accumbens Core and
670 Shell. Journal of Neuroscience 31:11786–11794.

671 D'Ambra AF, Jung SJ, Ganesan S, Antzoulatos EG, Fioravante D (2020) Cerebellar Activation
672 Bidirectionally Regulates Nucleus Accumbens Medial Shell and Core. Neuroscience.
673 Available at: http://biorxiv.org/lookup/doi/10.1101/2020.09.28.283952.

674 Dempesy CW, Tootle DM, Fontana CJ, Fitzjarrell AT, Garey RE, Heath RG (1983) Stimulation
675 of the paleocerebellar cortex of the cat: increased rate of synthesis and release of
676 catecholamines at limbic sites. Biol Psychiatry 18:127–132.

677 Dietrichs E, Haines DE (1989) Interconnections between hypothalamus and cerebellum.
678 Anatomy and Embryology 179:207–220.

679 D'Mello AM, Stoodley CJ (2015) Cerebro-cerebellar circuits in autism spectrum disorder.
680 Frontiers in Neuroscience 9 Available at:
681 http://journal.frontiersin.org/Article/10.3389/fnins.2015.00408/abstract.

682 Ernst M (2002) Decision-making in a Risk-taking Task A PET Study.
683 Neuropsychopharmacology 26:682–691.

684 Ernst TM, Brol AE, Gratz M, Ritter C, Bingel U, Schlamann M, Maderwald S, Quick HH, Merz
685 CJ, Timmann D (2019) The cerebellum is involved in processing of predictions and
686 prediction errors in a fear conditioning paradigm. eLife 8 Available at:
687 https://elifesciences.org/articles/46831.

688 Floresco SB (2015) The Nucleus Accumbens: An Interface Between Cognition, Emotion, and
689 Action. Annual Review of Psychology 66:25–52.

690 Floresco SB, Montes DR, Tse MMT, van Holstein M (2018) Differential Contributions of
691 Nucleus Accumbens Subregions to Cue-Guided Risk/Reward Decision Making and
692 Implementation of Conditional Rules. The Journal of Neuroscience 38:1901–1914.

693 Flores-Dourojeanni JP, van Rijt C, van den Munkhof MH, Boekhoudt L, Luijendijk MCM,
694 Vanderschuren LJMJ, Adan RAH (2021) Temporally Specific Roles of Ventral
695 Tegmental Area Projections to the Nucleus Accumbens and Prefrontal Cortex in
696 Attention and Impulse Control. J Neurosci 41:4293–4304.

697 Frontera JL, Baba Aissa H, Sala RW, Mailhes-Hamon C, Georgescu IA, Léna C, Popa D
698 (2020) Bidirectional control of fear memories by cerebellar neurons projecting to the
699 ventrolateral periaqueductal grey. Nature Communications 11 Available at:
700 http://www.nature.com/articles/s41467-020-18953-0.

701 Fujita H, Kodama T, du Lac S (2020) Modular output circuits of the fastigial nucleus for diverse
702 motor and nonmotor functions of the cerebellar vermis Orr HT, Ivry RB, De Zeeuw CI,
703 Sillitoe RV, eds. eLife 9:e58613.

704 Gao Z, Davis C, Thomas AM, Economo MN, Abrego AM, Svoboda K, De Zeeuw CI, Li N
705 (2018) A cortico-cerebellar loop for motor planning. Nature 563:113–116.

706 Garris PA, Kilpatrick M, Bunin MA, Michael D, Walker QD, Wightman RM (1999) Dissociation
707 of dopamine release in the nucleus accumbens from intracranial self-stimulation. Nature
708 398:67–69.

709 Gornati SV, Schäfer CB, Eelkman Rooda OHJ, Nigg AL, De Zeeuw CI, Hoebeek FE (2018)
710 Differentiating Cerebellar Impact on Thalamic Nuclei. Cell Rep 23:2690–2704.

711 Grill WM, Cantrell MB, Robertson MS (2008) Antidromic propagation of action potentials in
712 branched axons: implications for the mechanisms of action of deep brain stimulation. J
713 Comput Neurosci 24:81–93.

714 Groenewegen HJ, Wright CI, Beijer AV, Voorn P (1999) Convergence and segregation of
715 ventral striatal inputs and outputs. Ann N Y Acad Sci 877:49–63.

716 Guo Z, Chen J, Liu S, Li Y, Sun B, Gao Z (2013) Brain areas activated by uncertain reward-
717 based decision-making in healthy volunteers. Neural Regen Res 8:3344–3352.

718 Han X, Jing M, Zhao T, Wu N, Song R, Li J (2017) Role of dopamine projections from ventral
719 tegmental area to nucleus accumbens and medial prefrontal cortex in reinforcement
720 behaviors assessed using optogenetic manipulation. Metab Brain Dis 32:1491–1502.

721 Hara M, Sasa M, Takaori S (1989) Ventral tegmental area-mediated inhibition of neurons of
722 the nucleus accumbens receiving input from the parafascicular nucleus of the thalamus
723 is mediated by dopamine D1 receptors. Neuropharmacology 28:1203–1209.

724 Heath RG, Dempesy CW, Fontana CJ, Myers WA (1978) Cerebellar stimulation: effects on
725 septal region, hippocampus, and amygdala of cats and rats. Biol Psychiatry 13:501–
726 529.

727 Heffley W, Hull C (2019) Classical conditioning drives learned reward prediction signals in
728 climbing fibers across the lateral cerebellum. eLife 8 Available at:
729 https://elifesciences.org/articles/46764.

730 Hendry SHC, Jones EG, Graham J (1979) Thalamic relay nuclei for cerebellar and certain
731 related fiber systems in the cat. The Journal of Comparative Neurology 185:679–713.

732 Holloway ZR, Paige NB, Comstock JF, Nolen HG, Sable HJ, Lester DB (2019) Cerebellar
733 Modulation of Mesolimbic Dopamine Transmission Is Functionally Asymmetrical. The
734 Cerebellum 18:922–931.

735 Holtzman-Assif O, Laurent V, Westbrook RF (2010) Blockade of dopamine activity in the
736 nucleus accumbens impairs learning extinction of conditioned fear. Learn Mem 17:71–
737 75.

738 Hull C (2020) Prediction signals in the cerebellum: beyond supervised motor learning. eLife 9
739 Available at: https://elifesciences.org/articles/54073.

740 Ikemoto S (2007) Dopamine reward circuitry: Two projection systems from the ventral midbrain
741 to the nucleus accumbens–olfactory tubercle complex. Brain Research Reviews 56:27–
742 78.

743 Ito M (2006) Cerebellar circuitry as a neuronal machine. Prog Neurobiol 78:272–303.

744 Ito M (2008) Control of mental activities by internal models in the cerebellum. Nature Reviews
745 Neuroscience 9:304–313.

746 Ito R, Hayen A (2011) Opposing Roles of Nucleus Accumbens Core and Shell Dopamine in
747 the Modulation of Limbic Information Processing. Journal of Neuroscience 31:6001–
748 6007.

749 Jackman SL, Chen CH, Offermann HL, Drew IR, Harrison BM, Bowman AM, Flick KM, Flaquer
750 I, Regehr WG (2020) Cerebellar Purkinje cell activity modulates aggressive behavior.
751 eLife 9 Available at: https://elifesciences.org/articles/53229.

752 Jones EG, Leavitt RY (1974) Retrograde axonal transport and the demonstration of non-
753 specific projections to the cerebral cortex and striatum from thalamic intralaminar nuclei
754 in the rat, cat and monkey. J Comp Neurol 154:349–377.

755 Judd EN, Lewis SM, Heck DG, Person AL (2021) Widespread inhibitory projections from the
756 interposed cerebellar nucleus. Neuroscience. Available at:
757 http://biorxiv.org/lookup/doi/10.1101/2020.12.31.425011.

758 Jung SJ, Vlasov K, D'Ambra AF, Parigi A, Baya M, Frez EP, Villalobos J, Fernandez-Frentzel
759 M, Anguiano M, Ideguchi Y, Antzoulatos EG, Fioravante D (2022) Novel Cerebello-
760 Amygdala Connections Provide Missing Link Between Cerebellum and Limbic System.
761 Front Syst Neurosci 16:879634.

762 Kato S, Nishizawa K, Kobayashi K (2021) Thalamostriatal System Controls the Acquisition,
763 Performance, and Flexibility of Learning Behavior. Front Syst Neurosci 15:729389.

764 Kelland MD, Chiodo LA, Freeman AS (1991) Dissociative anesthesia and striatal neuronal
765 electrophysiology. Synapse 9:75–78.

766 Kelly E et al. (2020) Regulation of autism-relevant behaviors by cerebellar–prefrontal cortical
767 circuits. Nature Neuroscience Available at: http://www.nature.com/articles/s41593-020-
768 0665-z.

769 Klawonn AM, Malenka RC (2018) Nucleus Accumbens Modulation in Reward and Aversion.
770 Cold Spring Harbor Symposia on Quantitative Biology 83:119–129.

771 Kostadinov D, Beau M, Pozo MB, Häusser M (2019) Predictive and reactive reward signals
772 conveyed by climbing fiber inputs to cerebellar Purkinje cells. Nature Neuroscience
773 22:950–962.

774 Kutlu MG, Zachry JE, Melugin PR, Cajigas SA, Chevee MF, Kelly SJ, Kutlu B, Tian L, Siciliano
775 CA, Calipari ES (2021) Dopamine release in the nucleus accumbens core signals
776 perceived saliency. Current Biology 31:4748-4761.e8.

777 Lanius RA, Rabellino D, Boyd JE, Harricharan S, Frewen PA, McKinnon MC (2017) The innate
778 alarm system in PTSD: conscious and subconscious processing of threat. Current
779 Opinion in Psychology 14:109–115.

780 Larry N, Yarkoni M, Lixenberg A, Joshua M (2019) Cerebellar climbing fibers encode expected
781 reward size. eLife 8 Available at: https://elifesciences.org/articles/46870 [Accessed
782 September 28, 2020].

783 Li Z, Chen Z, Fan G, Li A, Yuan J, Xu T (2018) Cell-Type-Specific Afferent Innervation of the
784 Nucleus Accumbens Core and Shell. Frontiers in Neuroanatomy 12 Available at:
785 https://www.frontiersin.org/article/10.3389/fnana.2018.00084/full.

786 Liang KJ, Carlson ES (2019) Resistance, vulnerability and resilience: A review of the cognitive
787 cerebellum in aging and neurodegenerative diseases. Neurobiology of Learning and
788 Memory Available at: https://linkinghub.elsevier.com/retrieve/pii/S107474271930005X.

789 Liu C, Goel P, Kaeser PS (2021) Spatial and temporal scales of dopamine transmission. Nat
790 Rev Neurosci 22:345–358.

791 Loriaux AL, Roitman JD, Roitman MF (2011) Nucleus accumbens shell, but not core, tracks
792 motivational value of salt. Journal of Neurophysiology 106:1537–1544.

793 Lorivel T, Roy V, Hilber P (2014) Fear-related behaviors in Lurcher mutant mice exposed to a
794 predator. Genes Brain Behav 13:794–801.

795 Low AYT et al. (2021) Reverse-translational identification of a cerebellar satiation network.
796 Nature Available at: https://www.nature.com/articles/s41586-021-04143-5.

797 Luo R, Uematsu A, Weitemier A, Aquili L, Koivumaa J, McHugh TJ, Johansen JP (2018) A
798 dopaminergic switch for fear to safety transitions. Nature Communications 9 Available
799 at: http://www.nature.com/articles/s41467-018-04784-7.

800 Ma M, Futia GL, de Souza FMS, Ozbay BN, Llano I, Gibson EA, Restrepo D (2020) Molecular
801 layer interneurons in the cerebellum encode for valence in associative learning. Nature
802 Communications 11 Available at: http://www.nature.com/articles/s41467-020-18034-2.

803 Mahon S (2001) Relationship between EEG Potentials and Intracellular Activity of Striatal and
804 Cortico-striatal Neurons: an In Vivo Study under Different Anesthetics. Cerebral Cortex
805 11:360–373.

806 Mateus J, Lopes C, Aroso M, Costa A, Gerós A, Meneses J, Faria P, Neto E, Lamghari M,
807 Sousa M, Aguiar P (2021) Bidirectional flow of action potentials in axons drives activity
808 dynamics in neuronal cultures. J Neural Eng 18:066045.

809 Medina JF (2019) Teaching the cerebellum about reward. Nature Neuroscience 22:846.

810 Miquel M, Vazquez-Sanroman D, Carbo-Gas M, Gil-Miravet I, Sanchis-Segura C, Carulli D,
811 Manzo J, Coria-Avila GA (2016) Have we been ignoring the elephant in the room?
812 Seven arguments for considering the cerebellum as part of addiction circuitry.
813 Neuroscience & Biobehavioral Reviews 60:1–11.

814 Mittleman G, Goldowitz D, Heck DH, Blaha CD (2008) Cerebellar modulation of frontal cortex
815 dopamine efflux in mice: relevance to autism and schizophrenia. Synapse 62:544–550.

816 Mohebi A, Pettibone JR, Hamid AA, Wong J-MT, Vinson LT, Patriarchi T, Tian L, Kennedy RT,
817 Berke JD (2019) Dissociable dopamine dynamics for learning and motivation. Nature
818 Available at: http://www.nature.com/articles/s41586-019-1235-y.

819 Moulton EA, Elman I, Becerra LR, Goldstein RZ, Borsook D (2014) The cerebellum and
820 addiction: insights gained from neuroimaging research. Addict Biol 19:317–331.

821 Oades RD, Halliday GM (1987) Ventral tegmental (A10) system: neurobiology. 1. Anatomy and
822 connectivity. Brain Res 434:117–165.

823 Oden A, Wedel H (1975) Arguments for Fisher's Permutation Test. Ann Statist 3:518–520.

824 Otsuka S, Konno K, Abe M, Motohashi J, Kohda K, Sakimura K, Watanabe M, Yuzaki M
825 (2016) Roles of Cbln1 in Non-Motor Functions of Mice. J Neurosci 36:11801–11816.

826 Peterson TC, Villatoro L, Arneson T, Ahuja B, Voss S, Swain RA (2012) Behavior modification
827 after inactivation of cerebellar dentate nuclei. Behavioral Neuroscience 126:551–562.

828 Phillipson OT (1979) Afferent projections to the ventral tegmental area of Tsai and
829 interfascicular nucleus: A horseradish peroxidase study in the rat. The Journal of
830 Comparative Neurology 187:117–143.

831 Rabellino D, Densmore M, Théberge J, McKinnon MC, Lanius RA (2018) The cerebellum after
832 trauma: Resting-state functional connectivity of the cerebellum in posttraumatic stress
833 disorder and its dissociative subtype. Human Brain Mapping 39:3354–3374.

834 Reeber SL, Otis TS, Sillitoe RV (2013) New roles for the cerebellum in health and disease.
835 Frontiers in Systems Neuroscience 7 Available at:
836 http://journal.frontiersin.org/article/10.3389/fnsys.2013.00083/abstract.

837 Rochefort C, Arabo A, Andre M, Poucet B, Save E, Rondi-Reig L (2011) Cerebellum Shapes
838 Hippocampal Spatial Code. Science 334:385–389.

839 Root DH, Barker DJ, Estrin DJ, Miranda-Barrientos JA, Liu B, Zhang S, Wang H-L, Vautier F,
840 Ramakrishnan C, Kim YS, Fenno L, Deisseroth K, Morales M (2020) Distinct Signaling
841 by Ventral Tegmental Area Glutamate, GABA, and Combinatorial Glutamate-GABA
842 Neurons in Motivated Behavior. Cell Reports 32:108094.

843 Roy AK, Fudge JL, Kelly C, Perry JSA, Daniele T, Carlisi C, Benson B, Castellanos FX,
844 Milham MP, Pine DS, Ernst M (2013) Intrinsic functional connectivity of amygdala-based
845 networks in adolescent generalized anxiety disorder. J Am Acad Child Adolesc
846 Psychiatry 52:290-299.e2.

847 Sacchetti B, Baldi E, Lorenzini CA, Bucherelli C (2002) Cerebellar role in fear-conditioning
848 consolidation. Proc Natl Acad Sci USA 99:8406–8411.

849 Salgado S, Kaplitt MG (2015) The Nucleus Accumbens: A Comprehensive Review. Stereotact
850 Funct Neurosurg 93:75–93.

851 Sathyanesan A, Zhou J, Scafidi J, Heck DH, Sillitoe RV, Gallo V (2019) Emerging connections
852 between cerebellar development, behaviour and complex brain disorders. Nature
853 Reviews Neuroscience 20:298–313.

854 Schmahmann JD (2019) The cerebellum and cognition. Neuroscience Letters 688:62–75.

855 Shan Q, Hu Y, Chen S, Tian Y (2022) Nucleus accumbens dichotomically controls social
856 dominance in male mice. Neuropsychopharmacol 47:776–787.

857 Shuster SA, Wagner MJ, Pan-Doh N, Ren J, Grutzner SM, Beier KT, Kim TH, Schnitzer MJ,
858 Luo L (2021) The relationship between birth timing, circuit wiring, and physiological
859 response properties of cerebellar granule cells. Proc Natl Acad Sci USA
860 118:e2101826118.

861 Sippy T, Tritsch NX (2023) Unraveling the dynamics of dopamine release and its actions on
862 target cells. Trends in Neurosciences 46:228–239.

863 Snider RS, Maiti A (1976) Cerebellar contributions to the Papez circuit. J Neurosci Res 2:133–
864 146.

865 Sokolov AA, Miall RC, Ivry RB (2017) The Cerebellum: Adaptive Prediction for Movement and
866 Cognition. Trends in Cognitive Sciences 21:313–332.

867 Stamatakis AM, Jennings JH, Ung RL, Blair GA, Weinberg RJ, Neve RL, Boyce F, Mattis J,
868 Ramakrishnan C, Deisseroth K, Stuber GD (2013) A Unique Population of Ventral
869 Tegmental Area Neurons Inhibits the Lateral Habenula to Promote Reward. Neuron
870 80:1039–1053.

871 Strata P (2015) The Emotional Cerebellum. Cerebellum.

872 Strick PL, Dum RP, Fiez JA (2009) Cerebellum and Nonmotor Function. Annual Review of
873 Neuroscience 32:413–434.

874 Su H-S, Bentivoglio M (1990) Thalamic midline cell populations projecting to the nucleus
875 accumbens, amygdala, and hippocampus in the rat. The Journal of Comparative
876 Neurology 297:582–593.

877 Supple WF Jr, Leaton RN, Fanselow MS (1987) Effects of cerebellar vermal lesions on
878 species-specific fear responses, neophobia, and taste-aversion learning in rats. Physiol
879 Behav 39:579–586.

880 Taylor SR, Badurek S, Dileone RJ, Nashmi R, Minichiello L, Picciotto MR (2014) GABAergic
881 and glutamatergic efferents of the mouse ventral tegmental area: Mouse VTA
882 projections. Journal of Comparative Neurology 522:3308–3334.

Van der Werf YD, Witter MP, Groenewegen HJ (2002) The intralaminar and midline nuclei of the thalamus. Anatomical and functional evidence for participation in processes of arousal and awareness. Brain Res Brain Res Rev 39:107–140.

Volkow ND, Wang G-J, Tomasi D, Baler RD (2013) Unbalanced neuronal circuits in addiction. Current Opinion in Neurobiology 23:639–648.

Wagner MJ, Kim TH, Savall J, Schnitzer MJ, Luo L (2017) Cerebellar granule cells encode the expectation of reward. Nature Available at: http://www.nature.com/doifinder/10.1038/nature21726.

Wang SS-H, Kloth AD, Badura A (2014) The cerebellum, sensitive periods, and autism. Neuron 83:518–532.

Washburn S, Oñate M, Yoshida J, Vera J, K. B. R, Khatami L, Nadim F, Khodakhah K (2022) Cerebellum Directly Modulates the Substantia Nigra Dopaminergic Activity. Neuroscience. Available at: http://biorxiv.org/lookup/doi/10.1101/2022.05.20.492532.

Watabe-Uchida M, Zhu L, Ogawa SK, Vamanrao A, Uchida N (2012) Whole-Brain Mapping of Direct Inputs to Midbrain Dopamine Neurons. Neuron 74:858–873.

Watson TC, Becker N, Apps R, Jones MW (2014) Back to front: cerebellar connections and interactions with the prefrontal cortex. Frontiers in Systems Neuroscience 8 Available at: http://journal.frontiersin.org/article/10.3389/fnsys.2014.00004/abstract.

West EA, Carelli RM (2016) Nucleus Accumbens Core and Shell Differentially Encode Reward-Associated Cues after Reinforcer Devaluation. Journal of Neuroscience 36:1128–1139.

Xiao L, Scheiffele P (2018) Local and long-range circuit elements for cerebellar function. Current Opinion in Neurobiology 48:146–152.

Yamanaka K, Hori Y, Minamimoto T, Yamada H, Matsumoto N, Enomoto K, Aosaki T, Graybiel AM, Kimura M (2018) Roles of centromedian parafascicular nuclei of thalamus and cholinergic interneurons in the dorsal striatum in associative learning of environmental events. J Neural Transm 125:501–513.

Yang H, de Jong JW, Cerniauskas I, Peck JR, Lim BK, Gong H, Fields HL, Lammel S (2021) Pain modulates dopamine neurons via a spinal–parabrachial–mesencephalic circuit. Nat Neurosci 24:1402–1413.

Zahm DS (1999) Functional-anatomical Implications of the Nucleus Accumbens Core and Shell Subterritories. Annals of the New York Academy of Sciences 877:113–128.

Zeidler Z, Hoffmann K, Krook-Magnuson E (2020) HippoBellum: acute cerebellar modulation alters hippocampal dynamics and function. The Journal of Neuroscience:JN-RM-0763-20.

Zell V, Steinkellner T, Hollon NG, Warlow SM, Souter E, Faget L, Hunker AC, Jin X, Zweifel LS, Hnasko TS (2020) VTA Glutamate Neuron Activity Drives Positive Reinforcement Absent Dopamine Co-release. Neuron 107:864-873.e4.

Zingg B, Chou X, Zhang Z, Mesik L, Liang F, Tao HW, Zhang LI (2017) AAV-Mediated Anterograde Transsynaptic Tagging: Mapping Corticocollicular Input-Defined Neural Pathways for Defense Behaviors. Neuron 93:33–47.

926 **Figure legends**

927 **Figure 1. Cerebellar stimulation effectively elicits excitatory and inhibitory responses in**
928 **nucleus accumbens. A,** Schematic diagram of recording setup. Stimulation protocol consisted of 10
929 trials (inter-trial interval: 15 s) of five 100-μA, 0.5-ms pulses at 200 Hz. NAc: nucleus accumbens; CB:
930 cerebellum. **B**, Average spiking activity (spikes/s) across all recorded units (N = 42 mice). Inset shows
931 zoom-in of first two seconds after stimulation. **C**,**D**,**E**, Examples of excitatory (**C**), inhibitory (**D**), and
932 mixed (**E**) modulation in the NAc. *Top,* Peri-stimulus time histogram (PSTH) (10-ms bins) of the
933 average firing rate across 10 trials. *Bottom,* Baseline-normalized firing rate (z-score) across time.
934 *Inset*, Example average waveform of putative single unit. Scale bars: 1 ms, 10 μV. Shaded area
935 marks response window. **F,** Distribution of response types elicited in NAc by DCN stimulation. *Blue*:
936 Excitatory (E), *Red*: inhibitory (I), *Purple:* mixed, *Gray*: non-responders (NR). Number of recorded
937 units per response-type (*white*) and corresponding percentages are shown.

938 **Figure 2. Nucleus accumbens responses to cerebellar stimulation. A,** Recording sites in nucleus
939 accumbens core (NAc_{Core}) and medial shell (NAc_{Med}). Numbers indicate distance (in mm) from
940 bregma. **B,** Distribution of response types elicited by 30-, 100-, or 300-μA DCN stimulation. N_{30} = 14
941 mice, N_{100} = 42 mice, N_{300} = 40 mice. Outer ring (M): NAc_{Med}; inner ring (C): NAc_{Core}. *Blue:* excitatory
942 (E), *Red*: inhibitory (I), *Purple:* mixed, *Gray:* non-responders (NR). **C,** Comparison between average
943 baseline (Bsln) and peak firing rate (Resp) elicited by 100-μA DCN stimulation for excitatory
944 responses in NAc_{Core} (**C1**) and MAc_{Med} (**C2**). Group averages (± SEM) are overlaid onto lines
945 representing single units. **D1**,**2**, Same as C but for inhibitory responses.

946 **Figure 3. The distribution of response-types in nucleus accumbens subregions is not due to**
947 **topographical specialization within deep cerebellar nuclei. A**, The lateral (lat) or interposed (int)
948 DCN (**A1**) was electrically stimulated. M: medial n. **A2,** Demarcation of anatomical planes: ML:
949 medio-lateral; DV: dorsoventral; AP: antero-posterior. **B,C,** Stereotactic coordinates of DCN
950 stimulation sites in ML-DV (B1,C1), ML-AP (B2,C2), and AP-DV (B3,C3) planes. Colored dots denote
951 sites that evoked excitatory (excit.: *blue*), inhibitory (inh.: *red*), mixed (*purple*) or no responses (NR:
952 *gray*) in NAc_{Core} (B1-3) and NAc_{Med} (C1-3).

953 **Figure 4**. **Co-localization of nucleus accumbens-projecting neurons with cerebellar projections**
954 **in VTA and intralaminar thalamus**. **A**, Schematic diagrams of stereotactic injections in DCN and
955 NAc. **B1**, Expression of GFP at DCN injection sites. **B2**, Ctb-Alexa 568 injection site in NAc. **C**,

956 Overlap of ctb-labeled NAc projectors and DCN axons in VTA. **C1**, VTA identification through TH
957 immunostaining. **C2**, TH+ neuron. **C3**, Retrograde ctb-Alexa 568 labelling in NAc-projecting cell. **C4**,
958 GFP-expressing DCN axons. **C5**, C2-C4 merged. **D**, Overlap of ctb retrograde label (red) in NAc
959 projectors (blue; NeuN) and GFP-expressing DCN axons (green) in intralaminar thalamic nuclei. **D1**-
960 **D2**, Overlap in parafascicular (PF) n. **D3**-**D4**, Overlap in centromedial (CM) n. Yellow boxes in
961 C1,D1,D3 denote zoom-in areas depicted in C2-C5, D2 and D4, respectively. **E**-**F**, Airyscan confocal
962 images from experiments similar to **A** but with only lateral DCN injected with AAV-GFP. **E1**, Ctb-
963 labeled (red) NAc-projecting cell in the VTA. **E2,** TH+ cell (blue) with overlapping GFP-labeled axonal
964 projection (green) from lateral DCN. **E3,** E1-2 merged. **F1**, GFP-labeled axon from lateral DCN
965 (green) overlaps with ctb-labeled (red) NAc-projecting cell (blue: NeuN) in the PF n. **F2,** Same as in
966 F1 but for neuron in the CM n. Scale bars: B1-2,C1,D1: 200 μm; C2-C5,D2,D4,E1-3,F1,F2: 5 μm; D3:
967 100 μm. N = 6 mice. Numbers denote distance from bregma.

968 **Figure 5**. **Disynaptic cerebellum - nucleus accumbens connectivity is confirmed via**
969 **anterograde transsynaptic viral tracing**. **A**, Schematic diagram of AAV1-mediated transsynaptic
970 labeling approach. **B**, Schematic diagrams of stereotactic injections of floxed fluorophore in VTA and
971 thalamic nodes. **C1**, The VTA is visualized via TH immunostaining (green). Yellow box denotes zoom-
972 in area depicted in C2. Rn: red nucleus; ml: medial lemniscus. **C2**, Neurons that receive DCN input
973 are labeled with tdTomato (red; white arrowheads). Green: TH+ neurons (white arrows). Yellow
974 arrowhead: TH+, tdTomato+ neuron. **C3**, Projections of CB-VTA neurons in NAc_{Core} and NAc_{Med}. **D1**,
975 Neurons that receive DCN input in thalamus are labeled with tdTomato (red). Blue: NeuN. CM:
976 centromedial n.; PC: paracentral n.; CL: centrolateral n.; VL: ventrolateral n. **D2**, Same as D1, but for
977 parafascicular n. (PF). fr: fasciculus retroflexus. **D3**, Projections of CB-thalamic neurons in NAc_{Core}
978 and NAc_{Med}. **E**-**F**, Fluorescence images from experiments similar to A-B but with only lateral DCN
979 injected with AAV1-Cre. **E**, NAc projections of VTA neurons receiving input from lateral DCN. **F**,
980 Same as in E but for thalamic neurons. Scale bars below images: C1: 200 μm; C2: 100 μm; C3,D1-
981 3,E,F: 500 μm. N = 7 mice. Numbers denote distance from bregma.

982 **Figure 6. Photostimulation of cerebellar projections in VTA and thalamus elicits**
983 **responses in nucleus accumbens. A,** Schematic diagram of optophysiological approach.
984 *NAc:* nucleus accumbens, *CB:* cerebellum. **B,** Example ChR2-EYFP expression in DCN. lat:
985 lateral n.; ip: interposed n; m: medial n. **C**,**D**,**E**, Histology and NAc responses to optogenetic
986 stimulation of VTA (**C1**,**2**), CM (**D1**,**2**), and PF (**E1**,**2**). **C1**,**D1**,**E1**: Representative images of

987 optic fiber placement. ml: medial lemniscus; fr: fasciculus retroflexus. **C2**,**D2**,**E2**: Example
988 single units. *Left*: Average spike waveform. Scale bars: 1 ms, 10 μV. *Top*: PSTH (10-ms bins)
989 of firing rate (spikes/s). B*ottom*: Baseline-normalized firing rate (z-score) across time. Blue
990 lines denote photostimulation; Shaded area marks response window. Numbers below or next
991 to images indicate distance from bregma (in mm).

992 **Figure 7. Node-dependent differences in nucleus accumbens responses to photostimulation**
993 **of cerebellar projections. A1**,**B1**,**C1**, Average normalized activity (z-score) in NAc_{Core} (*top*) and
994 NAc_{Med} (*bottom*) as a function of time, for cerebellar fiber photostimulation (blue lines) in VTA (**A1**),
995 CM (**B1**) and PF (**C1**). **A2**,**B2**,**C2**, Distribution of response-types in NAc_{Core} (C: inner ring) and NAc_{Med}
996 (M: outer ring) upon photostimulation of cerebellar projections in VTA (**A2**), CM (**B2**), and PF (**C2**).
997 *Blue:* excitatory (E), *Red*: inhibitory (I), *Purple:* mixed, *Gray:* non-responders (NR). **D**, Average
998 normalized activity (z-score) in NAc_{Core} (*top*) and NAc_{Med} (*bottom*) as a function of time, for no-opsin
999 controls. **E**, Cumulative histogram of NAc response onset latencies upon cerebellar fiber
1000 photostimulation in VTA, CM and PF. Inset: 0-25 ms zoom-in. **F**,**G**,**H**, Violin plots of onset latencies of
1001 excitatory responses in NAc_{Core} (Core) and NAc_{Med} (Med), upon cerebellar fiber photostimulation in
1002 VTA (**F**), CM (**G**) and PF (**H**). Black lines: Median; White lines: interquartile range (Q1-Q3). VTA: N =
1003 4 mice, $n_{NAcCORE}$ = 22 units, n_{NAcMED} = 42 units; CM: N = 4 mice, $n_{NAcCORE}$ = 56 units, n_{NAcMED} = 26
1004 units; PF: N = 3 mice, $n_{NAcCORE}$ = 40 units, n_{NAcMED} = 20 units. D, no-opsin controls: N = 4 mice,
1005 $n_{NAcCORE}$ = 5 units, n_{NAcMED} = 36 units.

1006 **Table 1**. Percent responses in NAc_{Core} and NAc_{Med} elicited by photostimulation of cerebellar axons in
1007 VTA, CM and PF at different intensities.

1008 **Table 2**. Proportion of excitatory responses in NAc_{Core} and NAc_{Med} elicited by the first light pulse, at
1009 different photostimulation intensities.

1010

1011

Figure 1
D'Ambra et al., 2023

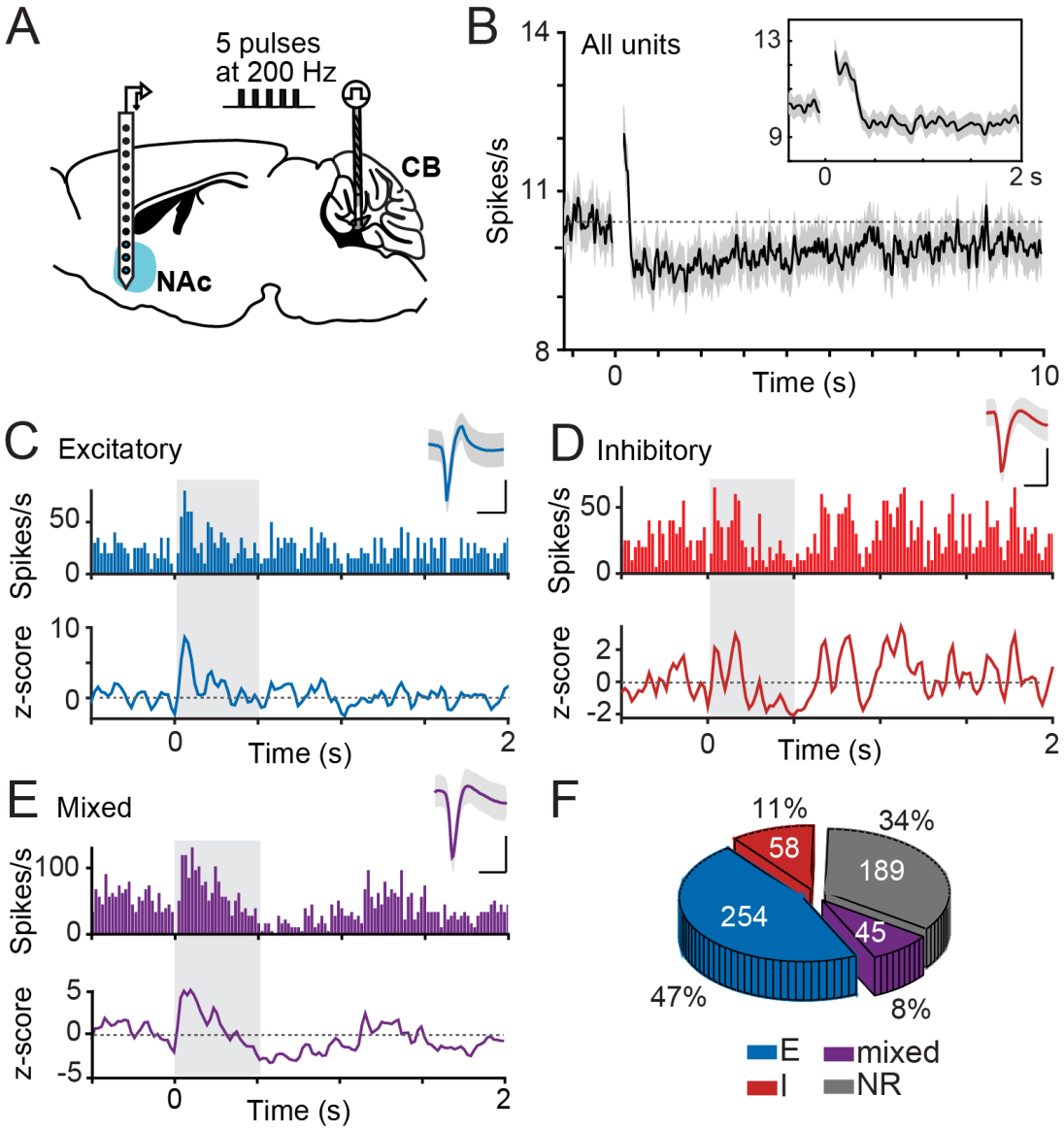

1031

1032

Figure 2
D'Ambra et al., 2023

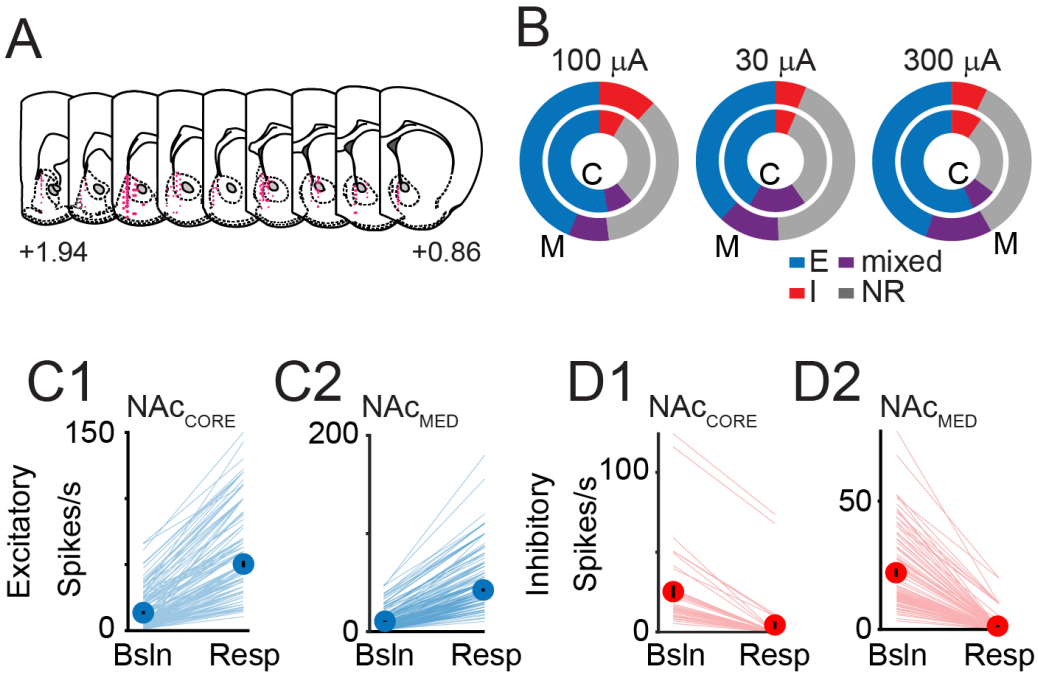

1033

Figure 3
D'Ambra et al., 2023

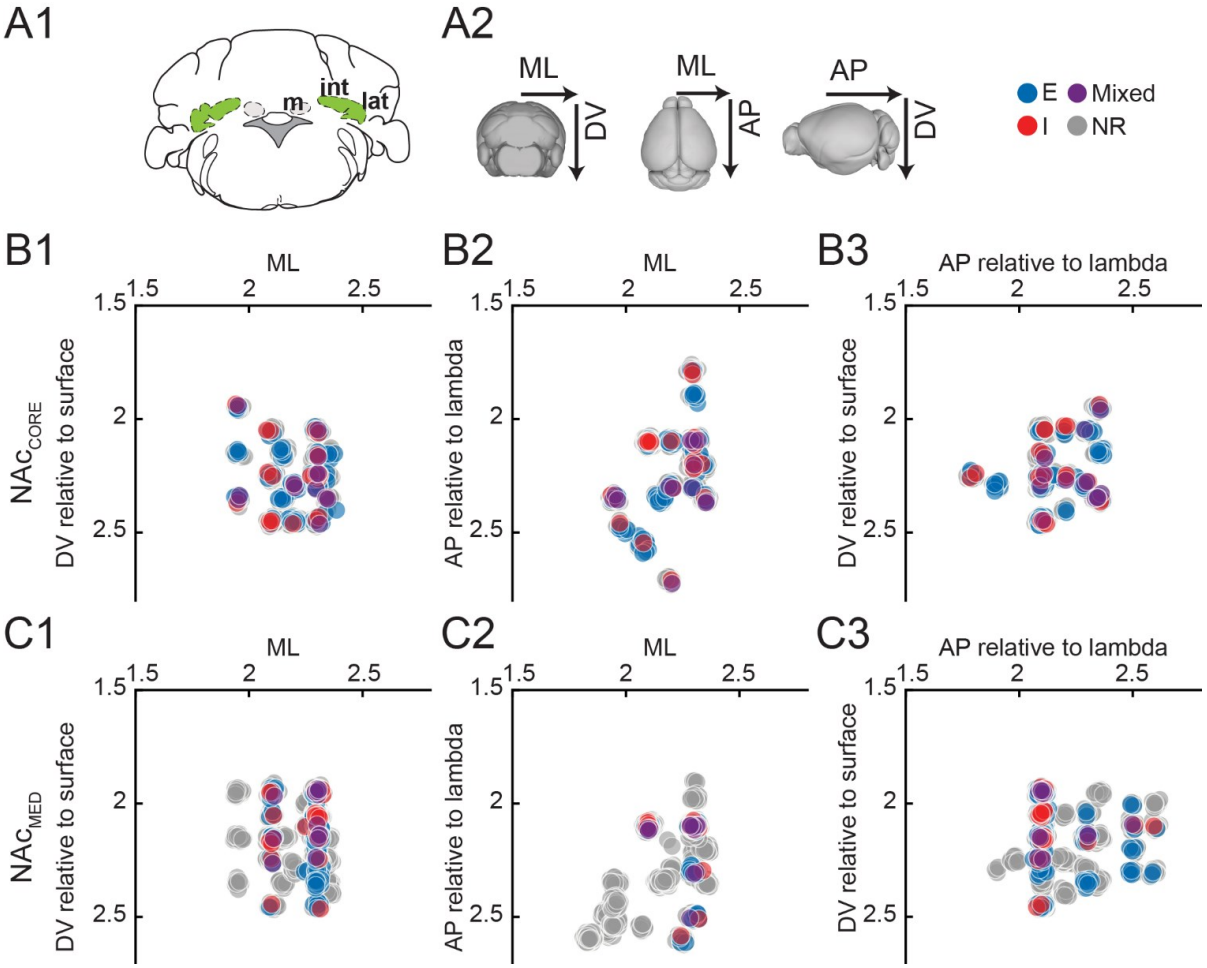

1034

Figure 4
D'Ambra et al. 2023

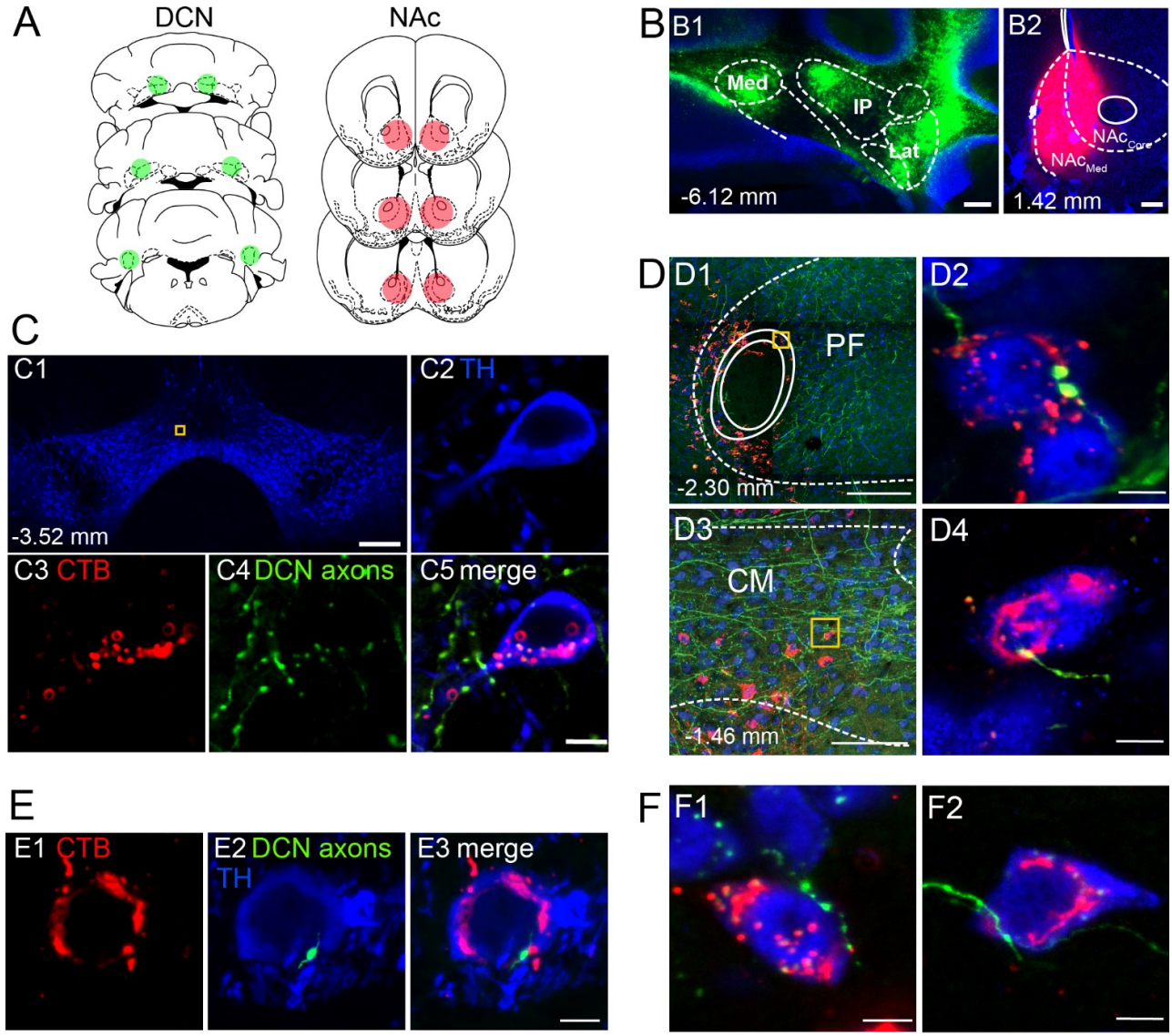

1035

Figure 5
D'Ambra et al., 2023

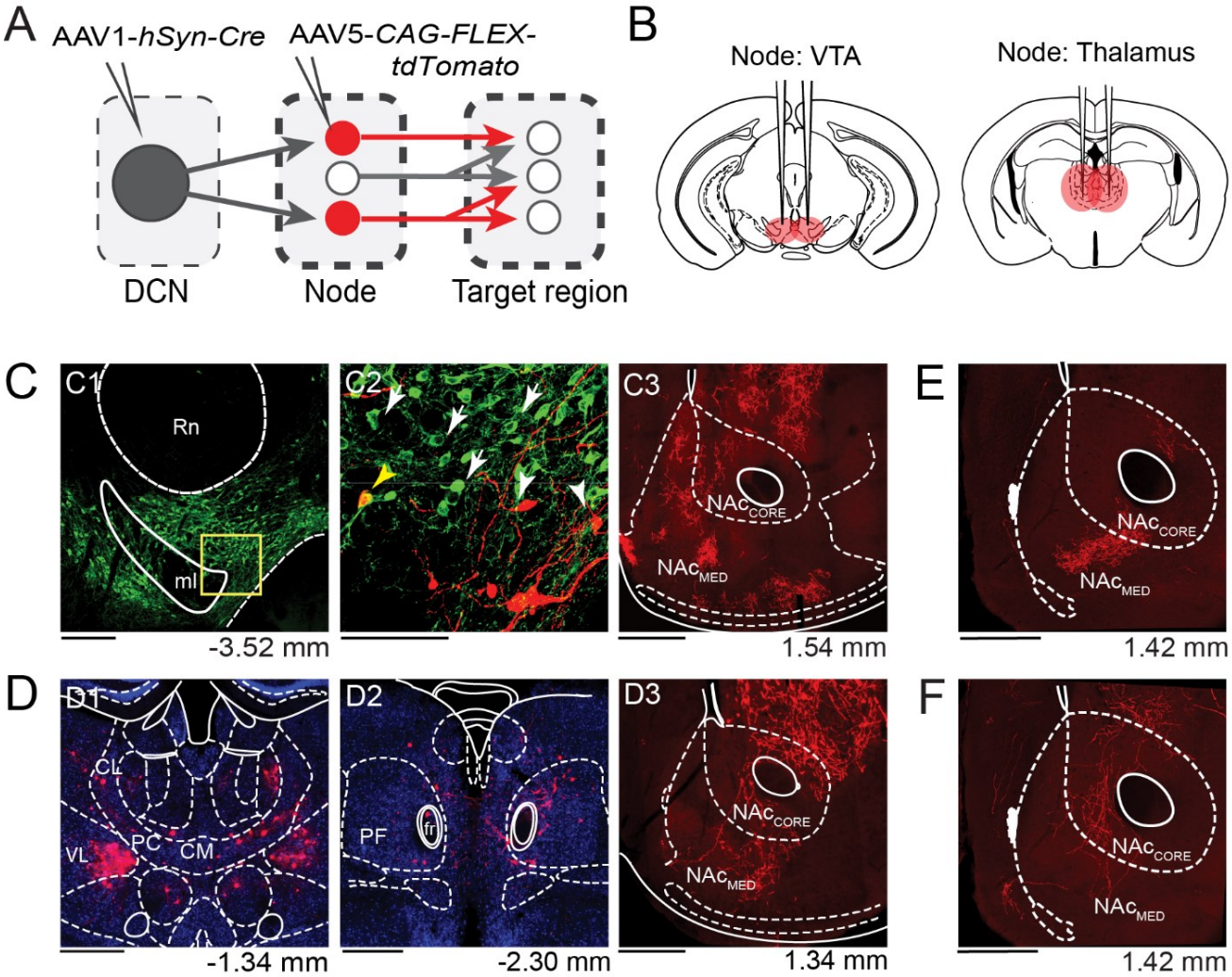

Figure 6
D'Ambra et al., 2023

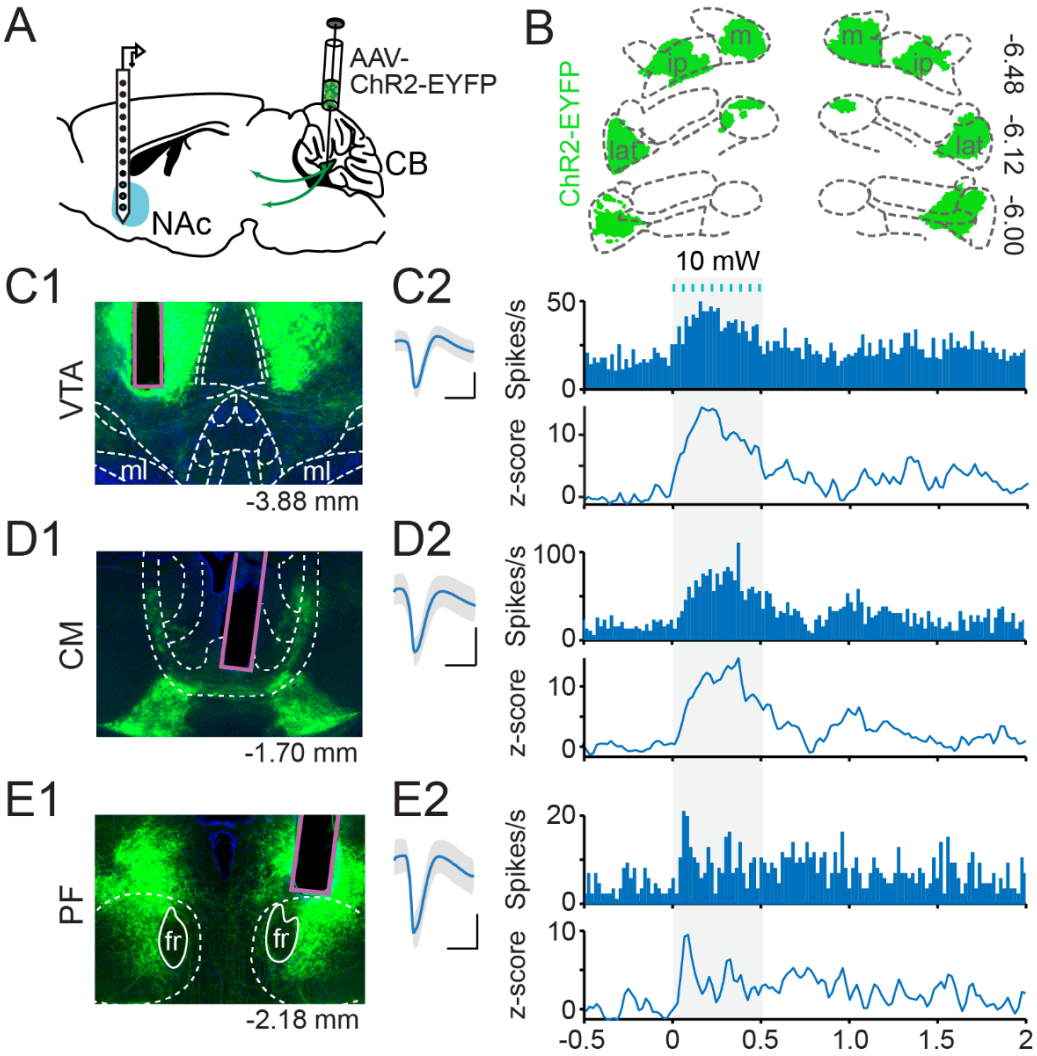

Figure 7
D'Ambra et al., 2023

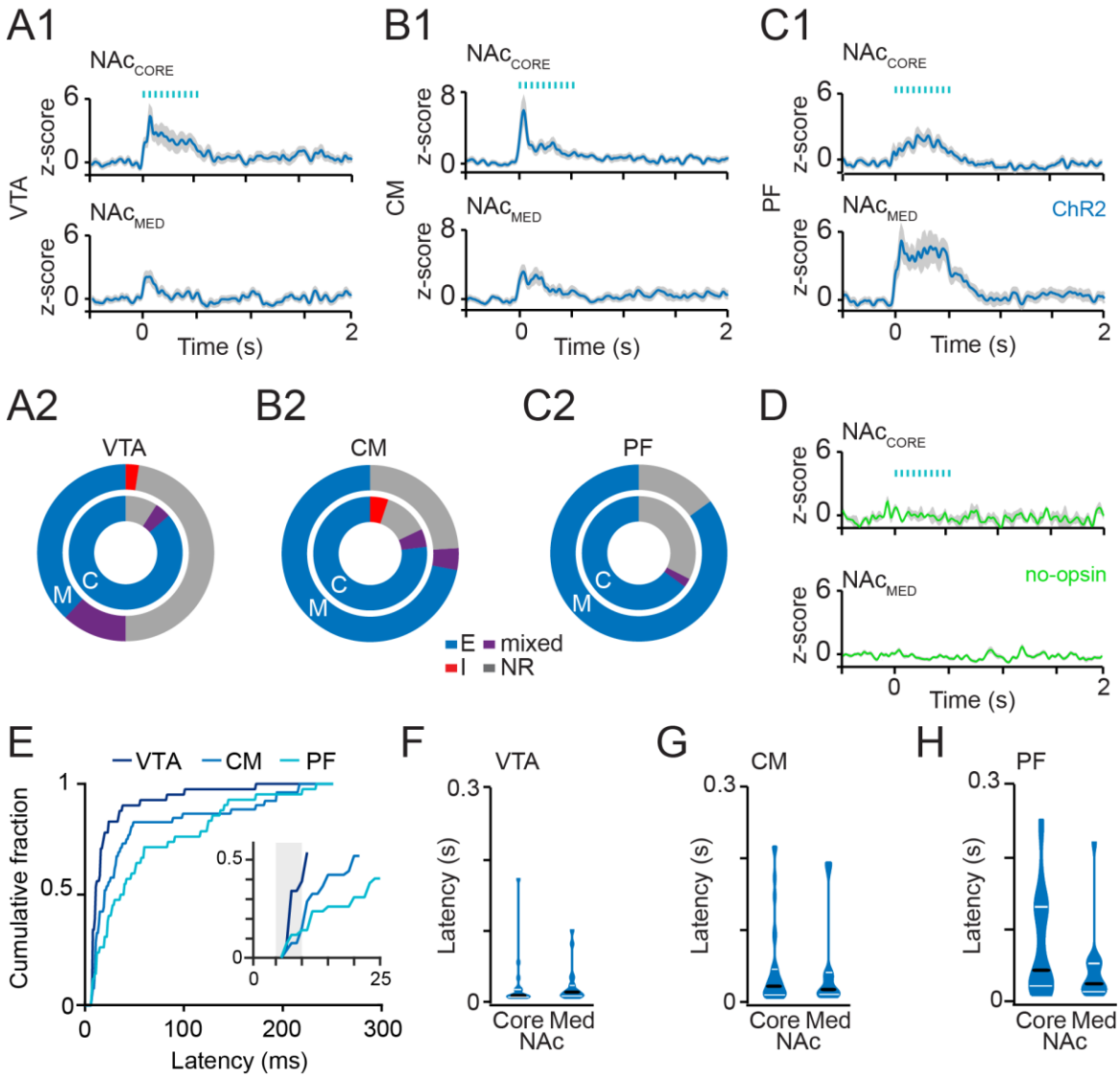

TABLE 1.

		Percent (%) responses					
		VTA		**CM**		**PF**	
Photostimulation Intensity		*NAc* $_{Core}$	*NAc* $_{Med}$	*NAc* $_{Core}$	*NAc* $_{Med}$	*NAc* $_{Core}$	*NAc* $_{Med}$
1 mW	Exc.	59	37	54	41	43	60
	Inh.	5	17	3	6	3	5
	Mixed	0	10	3	0	3	0
	No Res.	36	37	41	53	53	35
	n =	22	41	39	17	40	20
5 mW	Exc.	82	45	54	58	58	75
	Inh.	0	7	13	4	3	0
	Mixed	5	5	5	8	0	15
	No Res.	14	43	29	31	40	10
	n =	22	42	56	26	40	20
10 mW	Exc.	86	38	77	72	65	85
	Inh.	0	2	5	0	0	0
	Mixed	5	12	5	4	3	0
	No Res.	9	48	13	24	33	15
	n =	22	42	39	25	40	20

1077

TABLE 2.

		Proportion of responses elicited by 1st light pulse	
	Photostimulation Intensity	*NAc* $_{Core}$	*NAc* $_{Med}$
VTA	1 mW	7/13 (54%)	11/19 (58%)
	5 mW	16/19 (84%)	14/21 (67%)
	10 mW	18/20 (90%)	19/21 (90%)
CM	1 mW	16/22 (72%)	4/7 (57%)
	5 mW	27/33 (82%)	14/17 (82%)
	10 mW	26/32 (81%)	16/19 (84%)
PF	1 mW	12/18 (67%)	7/12 (58%)
	5 mW	15/23 (65%)	16/18 (89%)
	10 mW	14/27 (52%)	14/17 (82%)

1078